Cement and Concrete Research 201 (2026) 108123

Contents lists available at ScienceDirect

Cement and Concrete Research

journal homepage: www.elsevier.com/locate/cemconres

Impedance and electrical conductivity of C-S-H

Tulio Honorio [a,c,*], Walter Batista Bonfim [b], Oswaldo Cascudo [b]

[a] Université Paris-Saclay, CEA, Service de recherche en Corrosion et Comportement des Matériaux, 91191, Gif-sur-Yvette, France
[b] Universidade Federal de Goiás, Escola de Engenharia Civil e Ambiental, PPGGECON, Goiânia, Brazil
[c] Université Paris-Saclay, CentraleSupélec, ENS Paris-Saclay, CNRS, LMPS - Laboratoire de Mécanique Paris-Saclay, 91190, Gif-sur-Yvette, France

ARTICLE INFO

Keywords:
Electrical resistivity
Impedance
Molecular dynamics
Subdiffusion
Mean-field homogenization

ABSTRACT

The impedance and complex electrical conductivity of C-S-H have not been directly measured, even though electromagnetic measurements are a key non-destructive technique for probing cement systems. Here, we evaluate the frequency-dependent electrical conductivity of C-S-H using molecular dynamics simulations for the first time. The effect of nanopore size is assessed for pores spanning the interlayer to the gel range, showing that interlayer conductivity is governed by subdiffusive ion dynamics while Fickean dynamics drives gel pores behavior. Ionic self-correlations dominate the conductivity, while water–ion and solid–ion contributions are smaller but non-negligible. By combining molecular dynamics with mean-field homogenization, we obtain gel-scale estimates consistent with available data (i.e., with ratio between gel conductivity and pore solution conductivity on the order of 1/100). As with other transport properties, accounting for anisotropy and associated dimensionality loss is critical for understanding electrical conductivity bottom-up. Our results provide direct evaluation of the frequency-dependent conductivity of C-S-H, offering valuable input for multiscale modeling and for interpreting electromagnetic measurements of cementitious materials.

1. Introduction

Ion conductivity is the main mechanism responsible for the electrical conductivity of ordinary cement systems. Ions occupy the interlayer of C–S–H and are adsorbed onto the C–S–H surface in gel pores. These ions carry a net charge, potentially contributing to the direct-current (DC) electrical conductivity of cement-based materials. C–S–H is the major hydrated phase in these materials and generally functions as the host matrix mediating interactions among the other phases (including dielectric crystalline phases, other microporous phases, and porosity). Therefore, quantifying the electrical conductivity of C–S–H is critical for better interpret the results of electrical conductivity/resistivity of cement-based materials.

Direct measurements of DC conductivity for C–S–H remain unavailable; existing data are mostly derived from indirect or numerical analyses. Coverdale et al. [1] assumed a C–S–H conductivity of σ = 0.01 S/m in numerical simulations. Similarly, we previously reported a value of σ = 0.0246 S/m for all solids in cement pastes using a Monte Carlo micromechanical approach, with a standard deviation of 0.0384 S/m [2]. Ratios of C–S–H conductivity to pore-solution conductivity, σ/σ_{PS}, have been reported as 1/400 [3], 1/300 [4], 1/129 [5], and 1/121 [6]. Some studies utilize the equivalence of diffusivity and electrical conductivity via the Nernst–Einstein equation [4,6]. All these "top-down" approaches rely on inverse analyses and are inherently model-dependent, highlighting the need for direct, bottom-up evaluation of C–S–H conductivity. Recent DFT simulations [7] have begun to explore thermoelectric properties in related phases, yet the frequency-dependent electrical response of realistic C–S–H structures remains largely unexplored.

The molecular scale is the most relevant for understanding the origins of C–S–H's electrical response. Cations, primarily calcium, act as counterions balancing the net negative charge of C–S–H layers, forming inner-sphere complexes [8] or Stern layers within gel pores. These interlayer counterions contribute directly to C–S–H cohesion and mechanical strength [9]. Anions adsorbed onto surfaces form electrical double layers, with chloride, sulfate, carbonate, and hydroxide ions influencing conductivity and resistivity in concrete [10–12]. In the absence of flux correlations, the Nernst–Einstein equation describes electrolyte conductivity [13], but cross-correlations, ion–surface interactions, and solvent polarization also play important roles [14,15]. Confinement strongly affects ion transport and dielectric properties [16–20], and subdiffusive motion of calcium and hydroxide ions further reduces DC conductivity [16–18]. The combined effects of confinement, surface interactions, and subdiffusion on electrical conductivity remain an open question. Subdiffusive ionic motion is expected to significantly influence electrical conductivity in C–S–H, but these effects have not yet been explicitly addressed in the literature.

* Corresponding author at: Université Paris-Saclay, CEA, Service de recherche en Corrosion et Comportement des Matériaux, 91191, Gif-sur-Yvette, France.
E-mail address: tulio.honoriodefaria@cea.fr (T. Honorio).

https://doi.org/10.1016/j.cemconres.2025.108123
Received 15 September 2025; Received in revised form 19 November 2025; Accepted 16 December 2025
Available online 20 December 2025

Electrical conductivity is inherently frequency-dependent. Impedance spectroscopy is widely used for non-destructive testing, durability assessment, and early-age monitoring [21–24], including pore-size characterization [25]. Electrochemical techniques such as electrochemical impedance spectroscopy (EIS) and linear polarization resistance (LPR) also support the evaluation of steel corrosion in concrete [26]. A debate that spans decades persists regarding the origins of dispersion phenomena in impedance measurements, encompassing arguments related to ionic adsorption, ion-surface interactions, the nature of the electrical double layer, etc. [27]. Quantifying frequency-dependent electrical conductivity of C–S–H will thus provide crucial insights for interpreting impedance data and developing predictive models.

In this study, we address the lack of quantitative, multiscale data on the frequency-dependent electrical conductivity of C–S–H, which remains a critical gap for interpreting electromagnetic measurements and for developing physics-based multiscale models of cementitious materials. To fill this gap, we quantify the electrical conductivity and impedance of C–S–H at both the molecular and gel scales by combining molecular simulations with mean-field homogenization. At the molecular scale, we assess the sensitivity of direct-current and frequency-dependent conductivities to the choice of force field and decompose the contributions of ion self-interactions, ion–ion interactions, ion–surface interactions, and ion–solvent interactions within an anisotropic framework consistent with the layered structure of C–S–H. The influence of nanoscale confinement is examined by comparing conductivities obtained in confined and non-confined electrolyte systems. At the gel scale, effective conductivities are computed using established homogenization formulations, and the predicted values are compared with available experimental data. Finally, we propose a correction to account for the influence of pore-solution ions in cement systems. This integrated approach provides the first comprehensive, multiscale characterization of the electrical response of C–S–H suitable for engineering applications.

2. Molecular models and methods

2.1. Frequency-dependent electrical conductivity from molecular simulations

In the context of linear theory, the frequency-dependent electrical conductivity, denoted as $\sigma(f)$, can be computed using molecular simulations by cross-correlating the ion current $\vec{J}_I$ with the time derivative of total polarization $\dot{\vec{P}}$, as defined in the Green-Kubo expression [14,15,28]:

$$\sigma(f) = \frac{1}{V k_B T} \int_0^\infty e^{-2\pi i f t} \left\langle \vec{J}_I(0) \otimes \dot{\vec{P}}(t) \right\rangle dt \tag{1}$$

where V represents the volume probed, k_B is the Boltzmann constant, T is the temperature, t stands for time, and i denotes the imaginary unit. The tensor product $\otimes$ is deployed in the above expression to ensure its applicability to anisotropic systems as well. In cases of isotropic systems, this product simplifies to a scalar product of the vectors $\vec{J}_I$ and $\dot{\vec{P}}$. The expression above allow determining the frequency-dependent electrical conductivity of the system from the dynamics of the equilibrium fluctuations of ion flux current, which can be sampled in molecular dynamics simulations.

The ionic current $\vec{J}_I(t)$ is linked to the ionic polarization, with $\vec{J}_I(t) = \dot{\vec{P}}_I(t)$, and related to the electric field $\vec{E}$ through $\vec{J}_I(f) = \sigma(f)\epsilon_0\vec{E}(f)$. The frequency-dependent ionic conductivity can be split into real and imaginary components as follows:

$$\sigma(f) = \sigma'(f) + i\sigma''(f) \tag{2}$$

where σ' and σ'' represent the real and imaginary parts of the frequency-dependent ionic conductivity, respectively.

The total polarization $\vec{P}(t)$ is the cumulative sum of dipolar moments $\vec{\mu}$ of all N atoms in the system, given by:

$$\vec{P}(t) = \sum_i^N \vec{\mu}_i(t) = \sum_i^N q_i \vec{r}_i(t) \tag{3}$$

where $\vec{r}_i(t)$ indicates the position of atom i.

From these definitions, both $\vec{J}_I(t)$ and $\dot{\vec{P}}(t)$ can be computed during molecular simulations by summing up the velocities of particles $\vec{v}_i(t)$:

$$\dot{\vec{P}}(t) = \frac{d}{dt}\sum_i^N \vec{\mu}_i(t) = \sum_i^N q_i \frac{d\vec{r}_i(t)}{dt} = \sum_i^N q_i \vec{v}_i(t) \tag{4}$$

$$\vec{J}_I(t) = \frac{d}{dt}\sum_{i\in\text{ions}}^{N_{ions}} \vec{\mu}_i(t) = \sum_{i\in\text{ions}}^{N_{ions}} q_i \frac{d\vec{r}_i(t)}{dt} = \sum_{i\in\text{ions}}^{N_{ions}} q_i \vec{v}_i(t) \tag{5}$$

In the latter equation, the sum is performed over the N_{ions} ions present in the system.

In systems as C–S–H, composed of colloidal solid particles confining an electrolyte, the contributions to $\dot{\vec{P}}(t)$ and $\vec{J}_I(t)$ can be separated as follows:

$$\dot{\vec{P}}(t) = \dot{\vec{P}}_W(t) + \dot{\vec{P}}_S(t) + \vec{J}_I(t) \tag{6}$$

$$\vec{J}_I(t) = \vec{J}_{I+}(t) + \vec{J}_{I-}(t) \tag{7}$$

where the subscript W denotes the solvent, S the solid, and I represents the ions in the electrolyte, which can be anions ($I-$) or cations ($I+$).

The electrical conductivity can be decomposed into the following contributions:

$$\sigma(f) = \sigma_{II}(f) + \sigma_{IW}(f) + \sigma_{IS}(f) \tag{8}$$

where $\sigma_{II}(f)$ pertains to ion-ion correlations (or ion self-correlations), $\sigma_{IW}(f)$ corresponds to ion-solvent correlations, and $\sigma_{IS}(f)$ represents ion-solid correlations. For each contribution, the mathematical expressions are as follows:

$$\sigma_{II}(f) = \int_0^\infty \boldsymbol{\Phi}_{II} e^{-2\pi i f t} dt = \int_0^\infty \frac{\left\langle \vec{J}_I(0) \otimes \vec{J}_I(t) \right\rangle}{V k_B T} e^{-2\pi i f t} dt \tag{9}$$

$$\sigma_{IW}(f) = \int_0^\infty \boldsymbol{\Phi}_{IW} e^{-2\pi i f t} dt = \int_0^\infty \frac{\left\langle \vec{J}_I(0) \otimes \dot{\vec{P}}_W(t) \right\rangle}{V k_B T} e^{-2\pi i f t} dt \tag{10}$$

$$\sigma_{IS}(f) = \int_0^\infty \boldsymbol{\Phi}_{IS} e^{-2\pi i f t} dt = \int_0^\infty \frac{\left\langle \vec{J}_I(0) \otimes \dot{\vec{P}}_S(t) \right\rangle}{V k_B T} e^{-2\pi i f t} dt \tag{11}$$

In these equations, the cross-correlation functions $\boldsymbol{\Phi}_{II}$, $\boldsymbol{\Phi}_{IW}$, and $\boldsymbol{\Phi}_{IS}$ are defined based on the aforementioned correlations. In electrolytes with complex ionic compositions, the ionic flux can be deconstructed according to the total number of ionic types in the system. These expressions show that while only ion self and ion-ion correlations produce, by definition, ion fluxes, the correlations with solvent and solid atoms also contribute to the overall conductivity. A general expression for the correlations of species A and B per direction kl is given by:

$$\boldsymbol{\Phi}_{AB,kl}(t) = \int_0^\infty \frac{\left\langle \vec{J}_{A,kl}(0) \dot{\vec{P}}_{B,kl}(t) \right\rangle}{V k_B T} e^{-2\pi i f t} dt \tag{12}$$

The general anisotropic formulation provided above can be simplified for the case of slit pores. In a slit pore with an infinite fluid slab confined between two walls, the electrical conductivity tensor can be expressed as:

$$\sigma(f) = \begin{pmatrix} \sigma_\parallel(f) & 0 & 0 \\ 0 & \sigma_\parallel(f) & 0 \\ 0 & 0 & \sigma_\perp(f) \end{pmatrix} \tag{13}$$

where $\sigma_\parallel(f)$ represents the conductivity parallel to the pore plane, and $\sigma_\perp(f)$ represents the conductivity perpendicular to the slit pore

plane. This form assumes isotropy along the directions parallel to the pore plane. The out-of-diagonal components are expected to be negligible when the reference frame aligns with the pore plane. These assumptions are to be verified with the molecular simulations, specially for interlayer pores. As discussed in details for the case of the dielectric response [29,30], in the case of the slit geometry, the perpendicular component is to be computed as:

$$\sigma_{\perp}(f)^{-1} = \int_0^{\infty} \Phi_{T,zz} e^{-2\pi i f t} dt \tag{14}$$

where $\Phi_{T,zz}$ is the total correlation (including ion self, ion-ion, ion solvent and ion-surface correlations) computed for the z direction.

2.2. Impedance calculations

The impedance ($Z(f)$) can be expressed as a function of the complex conductivity as:

$$Z(f) = k\frac{1}{\sigma(f)} \tag{15}$$

where k is the cell constant, which converts conductivity, a material property, into impedance, a system property that includes physical dimensions. For a slit geometry, $k = l/A$ where l is the length of the pore and $A = w.d_{eff}$ is the cross-sectional area perpendicular to transport, where w is the pore width and d_{eff} is the pore thickness (or effective pore size) in the direction of the confinement. Assuming that C–S–H layers have disk shape morphology, as indicated by small-angle X-ray scattering (SAXS) experiments [31], the radius of the disk is $r = w = l$. The factor k in the expression above is then $k = 1/d_{eff}$.

2.3. Atomic structures, force fields and simulation details

We perform simulation in three kinds of system: calcium silicate hydrates at basal distance, electrolyte confined in C–S–H for various pore sizes, and representative bulk electrolytes as detailed below.

2.3.1. C–S–H models at basal spacing

The C–S–H atomistic model proposed by Kunhi et al. [32] with structural formula $1.67CaO.SiO_2.nH_2O$ is adopted. Two force fields are tested:

- ClayFF [33,34] using aqueous calcium ion parameters for interlayer Ca and hydroxide ion parameters. SPC/E [35] water model is chosen. This parametrization (called ClayFF Ca(aq)) used in previous works of ours as detailed in [36,37] yields good estimates of interfacial and thermoelastic properties of C–S–H.
- CSHFF [38], which adopts SPC water model [35].

In addition, we assess two other structures:

- Pellenq's C–S–H model [39], which has a similar Ca/Si ratio to the Kunhi et al. [32] model but was built differently, based on tobermorite 11 Å. The resulting basal spacing of around 11 Å is in better agreement with experiments [40] (that might refer however to dried conditions generally involved in C–S–H synthesis).
- Richardson's clinotobermorite 14 Å [40]. This structure is a fully crystalline structure shown to be a crystal-chemically plausible starting point for building C–S–H models.

These structures are also studied because they feature different contents of interlayer calcium and hydroxide (values gathered in Table 1), enabling the investigation of the influence of ion content in the interlayer. The simulations with these additional structures are only performed using the ClayFF force field.

ClayFF and CSHFF are non-polarizable force fields for classical molecular simulations. Therefore, effects associated with electronic conductivity cannot be captured by simulations using these force fields.

Table 1
Composition of calcium silicate hydrate models tested: C–S–H of Kunhi et al. [32], C–S–H of Pellenq et al. [39], and clinotobermorite 14 Å from Richardson [40]. Caw* and OH* refers to interlayer ions that are not balancing the solid layers charges (forming therefore $Ca(OH)_2$ clusters in the interlayer). For these calculations, we considered formal charges and not the partial charges from the force fields.

FF	C–S–H Kunhi et al.		C–S–H Pellenq et al.	Clinoto. 14 Å Richardson
	CSHFF	ClayFF	ClayFF	ClayFF
Si/Sim.	106		112	192
Ca/Si	1.67		1.68	0.83
Caw/Si	0.76		0.54	0.17
OH^-/Si	0.74		1.48	0.33
Water/Si	1.63		0.89	1.17
Caw*/Si	0.37		0.11	0
OH*/Si	0.74		0.63	0
Vol. [10^3 Å^3]	14.3	13.1	13.3	18.0
Dens. [g/cm^3]	2.35	2.55	2.53	2.32

Some classical force fields can account for polarization. But we highlight that the main mechanism associated with the conductivity of C–S–H is ionic conductivity, and, as will be discussed herein, diffusion plays a significant role. Simulation strategies that account for ion diffusion are therefore the most relevant. In this context, ClayFF and CSHFF are well suited for the task. Previous studies on other phyllosilicates have also used ClayFF to evaluate the electrical conductivity of confined electrolytes [41].

2.3.2. Electrolyte confined in C–S–H for various nanopores sizes

To evaluate the pore size dependence of the behavior of confined electrolytes, only the Kunhi et al. [32] C–S–H model is considered in simulations with the ClayFF Ca(aq) force field. This force field is better suited because it treats interlayer calcium and hydroxide as ions in aqueous solution, assigning their formal charges (+2e for calcium and -1e for hydroxide). Since ionic flux and current are directly related to charge, we believe that using the formal/full rather than partial charges, is more appropriate (however, we note that scaling of charges has been shown to better capture the behavior of some aqueous systems [42]. Such scaling, though, should be applied consistently within a dedicated study, which is beyond the scope of the current work.) The pores are constructed by varying the size of one of the interlayer pores in C–S–H, while the other is kept at the basal spacing, as in previous works [37,43,44]. The pore sizes tested span interlayer and gel pores, ranging from interlayer distances of 11.8 to 96.3 Å. The water content in these systems studied were obtained following Grand Canonical Monte Carlo (GCMC) simulations imposing a relative humidity of 100% under ambient conditions (300 K and 1 atm). Details of these simulations are given in previous studies [36,37].

2.3.3. Bulk electrolytes

The response of the non-confined electrolyte is also simulated using the same composition as the nanopore systems considered in the study of various nanopore sizes (the reference system Kunhi et al. [32] C–S–H model in simulations with the ClayFF). The atoms in the solid are deleted, and the system is re-equilibrated in NPT runs (using an isotropic barostat). After proper equilibration, the electrical conductivity is computed following the same protocol described below. The purpose of assessing the conductivity in the bulk system with the same composition as the confined system is to quantify the effect of confinement and separate the contribution of the interface on the electrical conductivity.

An additive model is used to distinguish the contribution of the interface, as previously employed in both experimental [45] and simulation [46] studies, with the total impedance being the sum of the

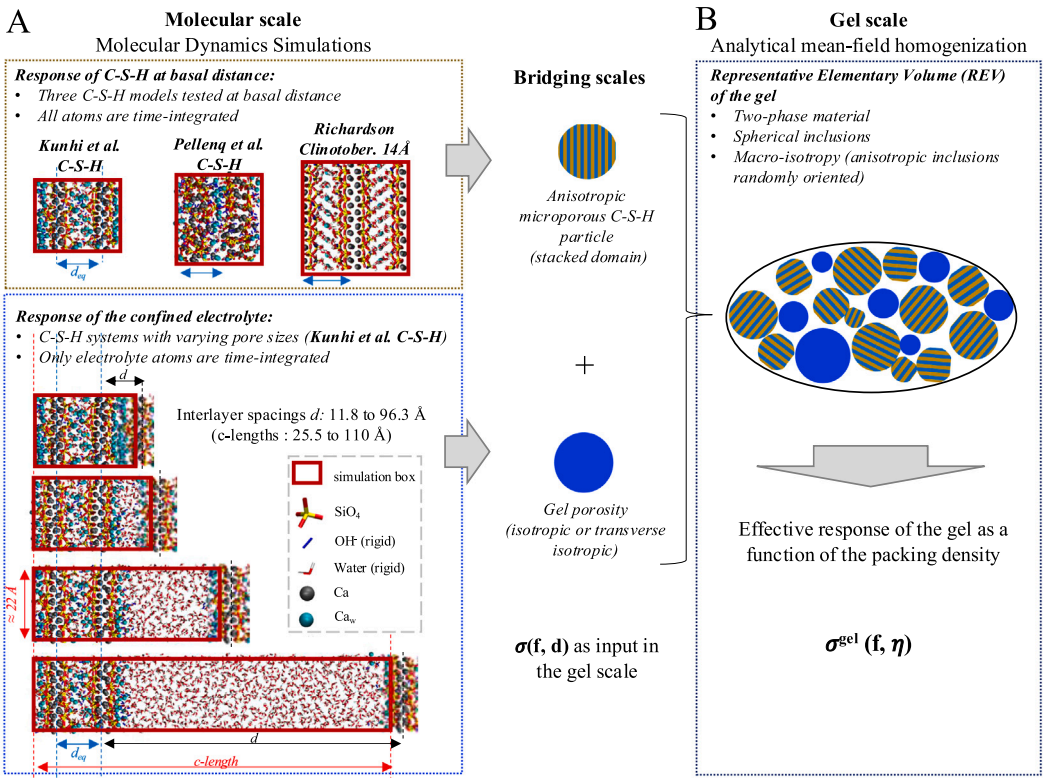

Fig. 1. Multiscale strategy integrating molecular simulations and mean-field homogenization to get the effective electrical conductivity of C–S–H. (A) Snapshot of the C–S–H atomic structures used in molecular simulations. (B) Microstructure representation of the gel scale adopted in the homogenization.
Source: Based in [18–20].

contributions from the bulk Z_{bulk} and the interfacial Z_{int} regions [45, 46]:

$$Z(f) = Z_{bulk}(f) + Z_{int}(f) \tag{16}$$

Similarly, the conductivity can be obtained as the sum of the inverses of the contributions of the bulk Z_{bulk} and the interfacial Z_{int} regions:

$$\frac{1}{\sigma(f)} = \frac{1}{\sigma_{bulk}(f)} + \frac{1}{\sigma_{int}(f)} \tag{17}$$

Simulations with bulk system also enable us to compare the dynamics of ions in bulk conditions with the one in confined systems, an aspect that will be critical to understand confined conductivity as discussed in the next section.

2.3.4. Simulation details

In all cases water molecules are constrained with SHAKE algorithm. Particle–particle particle-mesh solver (accuracy of 10^{-5}) is deployed to cope with long-range electrostatic interaction. Tail corrections are used for Lennard-Jones potential. Molecular simulations are performed with LAMMPS [47]. Fig. 1 shows a snapshot of the molecular systems simulated.

A timestep of 0.5 fs was adopted in the simulations to compute the electrical conductivity. The correlations were computed with LAMMPS's *fix ave/correlate* each 1 timestep in a 2000 timesteps window with calculated time window averages every 2000 timesteps. This time window is enough to capture the correlations decay (as can be seen in the results section) within a few picoseconds, which is a key information to define the upper limits of integration of correlation functions. Correlations were computed (with cumulation of correlations using *ave running*) in a 5 million timestep production run in the NVE ensemble after proper equilibration (first in NVT ensemble followed by NVE equilibration). The Fourier transforms of correlation functions are computed by numerical integration based on the results of molecular simulations. Twenty four trajectories are considered to calculate the average response and the standard error of system at basal spacing and confined electrolyte; five trajectories are considered for bulk electrolytes. The systems with the presence of a solid (basal spacing and confined electrolytes) required a larger number of trajectories to obtain sufficiently precise conductivity values, whereas for bulk systems, a smaller number of trajectories was sufficient to achieve similar precision. Only Oh dynamics is considered for OhHh correlations, i.e., the velocity of the hydrogen atom in the hydroxide ion is neglected and the total charge of the hydroxide ion is attributed to the Oh in the calculation of the ionic flux (the partial charge from the force field remains of course unaltered). This choice implies that the dynamics of the hydroxide ion is primarily driven by the Oh dynamics, which is consistent with the computation of the mean squared displacement (MSD) that tracks only Oh. Additionally, the dynamics of hydrogen atoms can exhibit large velocities in solids, leading to higher conductivities observed in confined fluids under highly constrained conditions (e.g., in interlayers and small gel pores). For this reason, the hydrogen dynamics are neglected in the calculation of hydroxide ionic flux. This choice is not significant for systems with Fickean dynamics (bulk systems or confined systems with larger mesopores), where results with or without accounting for hydrogen dynamics yield similar outcomes.

The volume in Eq. (1) is the *total simulation box* if one is interested in computing the electrical conductivity of C–S–H (including the solids layers) and bulk solutions. This volume can also be taken as the (effective) volume of the electrolyte in the interlayer if one is interested in the electrical conductivity of the electrolyte *confined in C–S–H*. In the later case, the volume of the electrolyte is evaluated using the sum of the Voronoï volume of interlayer species. Details are given in the Supporting Information A.

2.4. DC electrical conductivity from self-diffusion

The diffusion of interlayer calcium and hydroxide in C–S–H is shown to be subdiffusive [18], similar to the behavior of confined water in

interlayer and small gel pores [16–18]. Subdiffusion means that the mean-squared displacement (MSD) grows slower than linearly with time. Various phenomena are known to lead to subdiffusion, including notably fluid confinement [48]. In practice, subdiffusion of interlayer species in C–S–H translates into a time-dependent self-diffusion coefficient. Since conductivity is linked to diffusion, an expression that incorporates subdiffusive behavior into ionic conductivity should be provided.

Subdiffusion in interlayer species in C–S–H can be described using the generalized diffusion expression (e.g., [48,49]):

$$\langle r^2(t)\rangle \propto D_\alpha t^\alpha \tag{18}$$

In this power law, D_α is the generalized (or fractional) self-diffusion coefficient, α is the anomalous diffusion exponent, $\langle r^2(t)\rangle$ is the MSD, and t is the time. An $\alpha = 1$ signifies normal (Fickean) diffusion, while anomalous diffusion occurs when $\alpha > 1$ (superdiffusion) or $\alpha < 1$ (subdiffusion). The generalized diffusion coefficient D_α has dimensions of $[length^2.time^{-\alpha}]$, making it a "quasi-property" (i.e., defined by a ratio of physical quantities with non-integer exponents [50]). This quasi-property feature complicates comparisons between different D_α. To address this, a timescale-dependent diffusion coefficient can be defined using an Einstein-like equation [51]:

$$D_{t\to\tau} = \frac{1}{2d_s}\lim_{t\to\tau}\frac{\mathrm{MSD}(t)}{t} = \frac{1}{2d_s}\lim_{t\to\tau} D_\alpha t^{\alpha-1} \tag{19}$$

where τ is the timescale of interest and d_s is the dimensionality. This definition gives the diffusion coefficient the conventional units of diffusion provided that the timescale τ is specified.

With the definition in Eq. (19), the Nernst–Einstein equation can be generalized to account for power-law anomalous diffusion of species i $D_{i,t\to\tau}$:

$$\sigma^{NE}_{t\to\tau} = \frac{e^2}{k_B T}\sum_i^N z_i^2 c_i D_{i,t\to\tau} \tag{20}$$

where c_j is the molar concentration of ion i whose charge number is z_i.

In the Fickean case, self-diffusion in fully characterized by the velocity autocorrelation (e.g. [52]):

$$D_i = \frac{1}{2}\lim_{t\to\infty}\frac{\left\langle |\,\vec{r}_i(t)\,|^2\right\rangle}{t} = \int_0^\infty \left\langle \vec{v}_i(0).\vec{v}_i(t)\right\rangle dt \tag{21}$$

The comparison of Eq. (20) with Eqs. (21), shows that the DC conductivity given by and Eq. (1) can be then written as (e.g., [13]):

$$\sigma(f=0) = \sigma^{NE} + \sigma^X \tag{22}$$

where the second component account for mutual diffusion (associated with cross-velocity correlations):

$$\sigma^X = -\frac{e^2}{k_B T}\sum_i^N\sum_{j>i}^N z_i z_j c_i c_j D_{ij} \tag{23}$$

The calculations of Eq. (1) include these cross-correlations, but the estimates of $\sigma^{NE}_{t\to\tau}$ provided hereafter do not. Ion-ion and ion-surface correlations hinder charge diffusion, reducing the resulting ionic current. In the presence of ion-ion interaction, Nernst–Einstein leads therefore to an overestimation of the conductivity. The key difference from the original Nernst–Einstein equation is the introduction of a time-scale dependence due to anomalous diffusion. In the discussion of the results, we provide arguments demonstrating that neglecting this contribution in the case of subdiffusion is a pertinent choice, even considering that the effects coming from mutual diffusion are neglected.

The DC conductivity, evaluated using the generalized Nernst -Einstein equation, will be estimated based on the calculations of the MSD of interlayer species provided in our previous work [49] on the same C–S–H system studied here. This approach is significant because the calculation of conductivity using the Green-Kubo formalism primarily accounts for shorter timescales (as will be discussed in the results section), whereas the generalized Nernst–Einstein equation can incorporate much longer timescales, which are crucial for accurately determining DC conductivity under ultraconfinement conditions as in C–S–H interlayers.

2.5. Upscaling the complex conductivity

The micromechanical approach, based on mean-field analytical schemes, makes it possible to connect the composition and microstructure to the effective properties of the material. This methodology has recently been applied to the determination of mass transport properties [18,19] and dielectric permittivity [20] of C–S–H gels using input from molecular simulations. By mathematical analogy, the same strategy used for these conductivity-like properties can also be deployed for estimating electrical conductivity [53].

C–S–H is a heterogeneous phase whose microstructure can be modeled as a two-phase material constituted of microporous solid particles (representing solid C–S–H together with interlayers), and gel pores. This microstructure representation is depicted in Fig. 1, with the microporous particles being represented by transversely isotropic spherical inclusions, randomly distributed and oriented in a representative elementary volume (REV). Gel pore are also represented as spherical inclusions, and following the discussion in Ref. [20], might be seen as exhibiting an isotropic or transversely isotropic behavior - both cases will be considered here. This microstructure representation is supported by the inherent anisotropy of C–S–H, as evidenced by the significant difference in the order of magnitude of properties in the direction parallel to the microporous C–S–H layers (x and y) compared to the direction perpendicular to the plane (z) [18,20]. This approach makes it possible to upscale of information from the molecular scale to that of the gel, adequately accounting for anisotropy and heterogeneity, which are essential characteristics for modeling its effective properties of C–S–H [18,20].

A formulation based on the self-consistent scheme (or Bruggeman model) is used to describe the electrical behavior of C–S–H. Note that the most basic formulation of Bruggeman scheme deals with micro- and macro-isotropy; as discussed above, the formulation used here accounts for micro-anisotropy by considering at least one phase, microporous C–S–H, as a presenting transversely isotropic behavior. The macro-isotropy feature is kept. The self-consistent scheme treats all the phases as having the same status, unlike the Maxwell–Garnett model, for example, which assumes the existence of a hosting matrix in which the inclusions interact.

In this framework, the effective electrical conductivity, σ^{hom}, is described by an implicit equation that considers the anisotropy of two heterogeneous phases [18–20]:

$$\sigma^{hom} = \frac{\frac{7(1-f_g)\sigma_{\parallel,s}}{\sigma_{\parallel,s}+2\sigma^{hom}} + \frac{5(1-f_g)\sigma_{\perp,s}}{\sigma_{\perp,s}+\sigma^{hom}} - \frac{7f_g\sigma_{\parallel,g}}{\sigma_{\parallel,g}+\sigma^{hom}} - \frac{5f_g\sigma_{\perp,g}}{\sigma_{\perp,g}+2\sigma^{hom}}}{\frac{7(1-f_g)}{\sigma_{\parallel,s}+2\sigma^{hom}} + \frac{5(1-f_g)}{\sigma_{\perp,s}+2\sigma^{hom}} - \frac{7f_g}{\sigma_{\parallel,g}+2\sigma^{hom}} - \frac{5f_g}{\sigma_{\perp,g}+2\sigma^{hom}}} \tag{24}$$

where f_g represents the gel porosity, $\sigma_{\parallel,p} = \sigma_{x,p} = \sigma_{y,p}$, $\sigma_{z,p} = \sigma_{\perp,p}$ the subscripts $_{,s}$ and $_{,g}$ stand, respectively, for the solid C–S–H particle and gel porosity. Details of the derivation process of the expression above can be found in the Refs. [18,20]. The derivation of this equation is based on an Eshelby-type derivation, as proposed by Hatta et al. [54] for thermal conductivity problems. When solving the equation for the homogenized property, it is necessary to consider that multiple solutions may arise. However, only the root that produces positive results for DC conductivity was considered. This same root is then applied consistently when calculating the full complex spectra. Assuming that the conduction perpendicular to C–S–H layer in microporous C–S–H is zero $\sigma_{\perp,s} = 0$, Eq. (24) can be rewritten in the explicit forms below according to the following assumption regarding gel pore behavior:

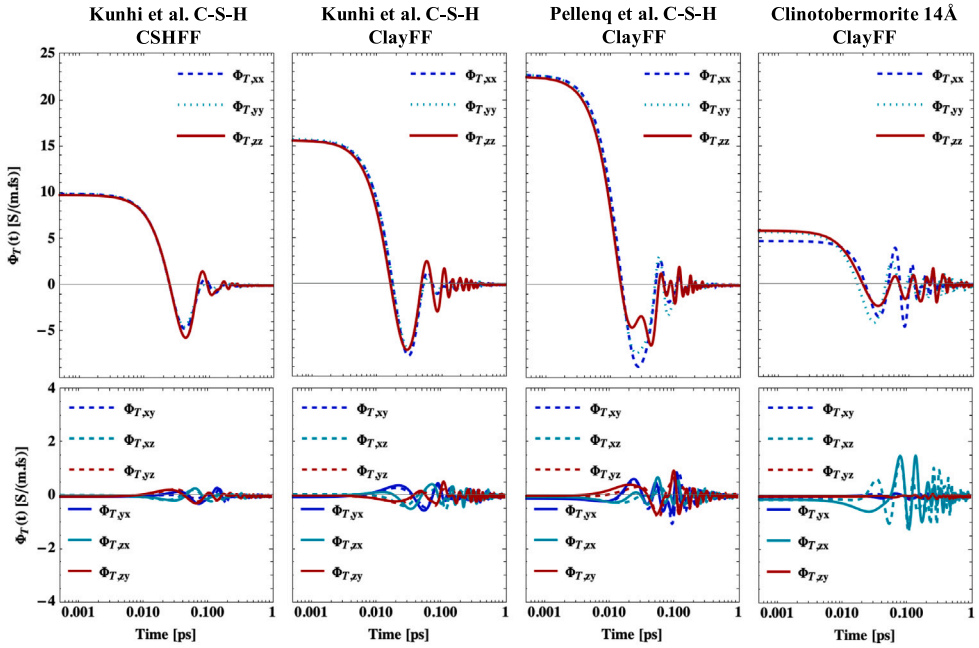

Fig. 2. Total correlation per direction kl for system at basal distance: comparison of simulations with Kunhi et al. [32] C–S–H model at basal spacing using ClayFF and CSHFF, Pellenq et al. C–S–H model and clinotobermorite 14 Å at basal spacing using ClayFF.

- *Isotropic behavior of gel pore*:

$$\sigma_{iso}^{hom} = \frac{1}{96}\left\{-A_{iso} + \sqrt{A_{iso}^2 - 192\left[15(1-f_g)\sigma_{\parallel,s}\sigma_g - 24\sigma_{\parallel,s}\sigma_g\right]}\right\} \tag{25}$$

where $A_{iso} = 24\sigma_{\parallel,s} - 42(1-f_g)\sigma_{\parallel,s} - 48\sigma_g + 72(1-f_g)\sigma_g$.

- *2D behavior of gel pore*:

$$\sigma_{2D}^{hom} = \frac{1}{96}\left\{-A_{2D} + \sqrt{1728\sigma_{\parallel,s}\sigma_{\parallel,g} + A_{2D}^2}\right\} \tag{26}$$

where $A_{2D} = 24\sigma_{\parallel,s} - 42(1-f_g)\sigma_{\parallel,s} - 18\sigma_g + 42(1-f_g)\sigma_g$ and we adopt $\sigma_{\perp,g} = 0$.

3. Results and discussion

3.1. Molecular scale

3.1.1. C–S–H at the basal distance

Ion self- and cross-correlations for all models tested (Kunhi et al. [32] C–S–H with ClayFF and CSHFF, Pellenq et al. C–S–H with ClayFF, and clinotobermorite 14 Å with ClayFF) are reported in the Supporting Information. All the correlations are well damped on the picosecond timescale, which corroborates the use of a picosecond as the upper integral limit in Eq. (1). All tested systems exhibit similar trends in all correlations but with remarkable differences. With the Kunhi et al. [32] C–S–H model, ion self-correlations show smaller amplitudes with CSHFF compared to ClayFF, which can be attributed to the lower absolute values of the partial charges of oxygen in CSHFF compared to ClayFF. Hydroxide correlations show a larger amplitude at low timescales than interlayer calcium in the Pellenq et al. C–S–H model compared with the Kunhi et al. [32] model and clinotobermorite. Interlayer calcium self-correlations are similar for the Kunhi et al. [32] and Pellenq et al. [39] C–S–H models simulated with ClayFF. Some level of anisotropy is observed, particularly for Caw simulated with ClayFF and in cross-correlations, where the zz correlations differ from the in-plane (xx and yy) correlations. The cross-correlations show a less pronounced contribution to the total correlation, with this contribution being more prominent in the 5 fs to 0.5 ps range. The amplitudes do not exceed −4 to 2 S/(m.fs), which is a fraction of the self-correlation amplitudes but still non-negligible.

The total correlations (including self- and cross-correlations) are shown in Fig. 2 per direction. The in-plane directions exhibit similar behavior justifying using as $\sigma_{\parallel}(f) = (\sigma_{xx}(f) + \sigma_{yy}(f))/2$ proposed in Eq. (13). A more pronounced anisotropy is observed in the axial direction in clinotobermorite. The off-diagonal directions show contributions that can be neglected, except for the xz direction in clinotobermorite, which exhibits correlations with the same amplitude as the axial directions. These results suggest that the fluxes are coupled along the xx and zz directions in clinotobermorite and that a frame aligned with the basal plane and the a-vector might not be the principal frame for this crystal. The symmetry of the response for the ij and ji components is verified to within a few units of S/(m.fs). The analysis of these results therefore suggests that the response in the form posited in Eq. (13) is relevant for C–S–H but might need to be revised for crystalline structures to achieve better accuracy. Herein, we assume Eq. (13) in the calculations, which should be seen as an approximate estimate for clinotobermorite.

The real $\sigma'_{kl}(f)$ and imaginary $\sigma''_{kl}(f)$ parts of the conductivity, as well as the associated Nyquist diagrams, are shown in the Supporting Information for the system tested. The values of DC conductivity obtained with Green-Kubo (GK) relation Eq. (1) are reported in Table 2. When all Ca^{2+} and OH^- in the interlayers are accounted for, the DC conductivity $\sigma_{\parallel}$ varies from 0.63 (Pellenq et al. C–S–H) to 7.32 S/m (clinotobermorite). These values are high compared to the expected values in the literature on the order of 0.01 S/m [2–6]. Even if this value refers to the gel scale, it can be shown using the homogenization formula in Section 2.5 that with conductivity for the microporous phase on the order of 1 S/m, it is not possible to obtain an effective conductivity for the gel on the order of 0.01 S/m, even when considering the dimensionality reduction due to the suppression of conductivity along the z-direction. Therefore, some explanations need to be proposed to account for the high conductivity values obtained using the fluctuation formula and to understand why the effective conductivity of microporous C–S–H is much lower in DC macroscopic measurements. Two hypotheses are proposed:

Table 2
Calculated DC electrical conductivity from Green-Kubo (GK) and Nernst–Einstein (NE) relations. For NE calculations, timescale-dependent diffusion coefficient $D_{t\to\tau}$ are used.

	C–S–H model:	Kunhi et al.		Pellenq et al.	Clinotober. 14 Å
	FF	CSHFF	ClayFF	ClayFF	ClayFF
$\sigma_{\parallel}$ [S/m]	GK all ions	2.82 ± 0.79	4.78 ± 0.85	0.63 ± 0.68	7.32 ± 0.28
	GK non-charge bal.	6.78 ± 0.81	2.97 ± 0.68	0.85 ± 0.25	0
	NE τ =1 ps[a] (THz scale)	7.78	5.07	2.71	1.26
	NE τ =1 ns[a] (GHz scale)	1.97E−02	2.31E−02	9.04E−03	4.31E−3
	NE τ =1 μs[a] (MHz scale)	1.73E−05	4.25E−05	9.00E−06	6.74E−06
	NE τ =1 ms[b] (kHz scale)	8.03E−08	6.72E−08	2.04E−08	5.06E−09
	NE τ =1 s[b] (Hz scale)	4.53E−11	1.44E−10	3.81E−11	8.98E−12

[a] Data from molecular simulations [49].
[b] Extrapolation from molecular simulation data. $D_{t\to\tau}$ was extrapolated by the potential fit with time; the estimated values were inserted into Eq. (20) to NE calculations [49].

Table 3
Diffusion of interlayer species at the basal spacing confinement: anomalous diffusion exponent α, generalized diffusion coefficient D_α, and timescale-dependent diffusion coefficient $D_{t\to\tau}$. The results are obtained with ClayFF and Kunhi et al. [32] C–S–H model. The values for xx and yy directions are shown in the Supporting Information.

		Species	Dir.	τ: 1 ps	1 ns	10 ns	0.1 μs	1 μs
C–S–H Kunhi et al. (ClayFF)	α	Oh	∥	0.24	0.02	0.01	0.06	0.17
		Caw	∥	0.25	0.01	0.00	0.01	0.04
	D_α [10^3 Å^2/ps$^\alpha$]	Oh	∥	4.2	11.8	11.5	12.7	6.1
		Caw	∥	2.3	11.2	9.0	7.5	7.0
	$D_{t\to\tau}$ [10^{-10} m^2/s]	Oh	∥	4.2E−01	1.3E−03	1.3E−04	2.5E−05	6.1E−06
		Caw	∥	2.3E−01	1.2E−03	9.1E−05	8.2E−06	1.3E−06
C–S–H Kunhi et al. (CSHFF)	α	Oh	∥	0.40	0.03	0.01	0.00	0.00
		Caw	∥	0.37	0.01	0.00	0.00	0.00
	D_α [10^3 Å^2/ps$^\alpha$]	Oh	∥	19.8	34.0	35.5	37.4	36.4
		Caw	∥	6.5	15.5	14.4	15.3	14.9
	$D_{t\to\tau}$ [10^{-10} m^2/s]	Oh	∥	2.0E+00	4.1E−03	4.0E−04	3.7E−05	3.6E−06
		Caw	∥	6.5E−01	1.7E−03	1.4E−04	1.5E−05	1.5E−06
C–S–H Pellenq et al.	α	Oh	∥	0.21	0.00	0.00	0.00	0.00
		Caw	∥	0.20	0.00	0.00	0.00	0.00
	D_α [10^3 Å^2/ps$^\alpha$]	Oh	∥	1.9	5.7	5.7	5.9	5.8
		Caw	∥	1.1	4.1	4.0	4.0	4.0
	$D_{t\to\tau}$ [10^{-10} m^2/s]	Oh	∥	1.9E−01	5.7E−04	5.7E−05	5.9E−06	5.8E−07
		Caw	∥	1.1E−01	4.1E−04	4.0E−05	4.0E−06	4.0E−07
Clinotobermorite 14 Å	α	Caw	∥	0.35	0.00	0.00	0.00	0.00
	D_α [10^3 Å^2/ps$^\alpha$]	Caw	∥	2.8	9.6	10.5	18.7	14.6
	$D_{t\to\tau}$ [10^{-10} m^2/s]	Caw	∥	2.8E−01	9.6E−04	1.1E−04	1.9E−05	1.5E−06

- *Hypothesis 1: Only ions that do not contribute to balancing the charge of the solid layers are available for ionic conductivity.* Only a part of the interlayer ions is required to balance the charge of the solid layers in some calcium silicate hydrates. The portion of the interlayer ions that does not balance the layer charge is reported in Table 1 for the systems studied. For the calculations, we considered formal charges and not the partial charges from the force fields. In clinotobermorite, all interlayer ions balance the solid layer charge. In both C–S–H models, the hydroxide in the interlayer does not balance the layer charge but instead balances additional Ca in the interlayer, added to reach a Ca/Si ratio of 1.67. In additional calculations of electrical conductivity, we account for the fraction of interlayer ions that do not balance the solid layers by multiplying the corresponding fraction into the calculation of correlation functions (case Green-Kubo (GK) non-charge balance). The values are compared with the conductivity with all ions in the interlayer (GK all ions case) in Table 2. Since the total correlation includes ion-ion correlation of cations and anions, introducing this calculation does not necessarily lead to a decrease in the estimated DC conductivity. A decrease is observed for the Kunhi et al. [32] C–S–H model with ClayFF. Of course, under this assumption, there is no ionic flux in clinotobermorite. An increase in DC conductivity is observed for the other cases. However, the order of magnitude of the DC conductivity remains the same, indicating that this hypothesis cannot explain the lower conductivity that would be expected based on macroscopic experimental evidence.
- *Hypothesis 2: Subdiffusion of ions hinders dynamics.* The dynamics of in C–S–H interlayers are shown to exhibit strongly subdiffusive behavior [16–18]. Table 3 gathers the self-diffusion coefficients of ionic interlayer species at the basal spacing confinement using the generalized diffusion description of Eq. (18) and the timescale-dependent diffusion coefficient $D_{t\to\tau}$ (Eq. (19)). The analysis of the anomalous diffusion exponent α shows that the diffusion of interlayer hydroxide and calcium in the C–S–H models and clinotobermorite is always subdiffusive, with $\alpha < 0.5$, which characterizes pronounced subdiffusion. For larger timescales, α decreases, indicating that the dynamics slow down over longer timescales. The order of magnitude of $D_{t\to\tau}$ at the microsecond scale is several orders smaller than the values of $D_{t\to\tau}$ at the picosecond scale. The GK estimates refer to the ps to ns scales; therefore, the diffusion (and consequently the conductivity) is

expected to be larger when evaluated at these timescales. For practical purposes of interpreting macroscopic measurements of DC conductivity, longer timescales must be accounted for. In Table 2, DC conductivity is also reported for timescales on the order of picoseconds (THz), microseconds (MHz), and seconds (Hz). The latter is obtained from the extrapolation of self-diffusion data. The values obtained at the second scale are significantly smaller. This results shows that ionic conductivity of interlayer species is very small in DC experiments (but not necessarily in frequency-dependent experiments as discussed hereafter).

The second hypothesis therefore suggests that the electrical conductivity of species in the interlayer at low frequency is very small (and in a simplified approach can be considered as an effective insulator). In this context, Nernst–Einstein estimates accounting for diffusion provided a good estimation of the DC conductivity. As will be discussed in Section 2.5, the conductivity of the gel porosity will be the main factor responsible for the nonzero DC conductivity on the order of 0.01 S/m reported for C–S–H and solids in cement systems [2–6]. For larger frequencies, notably closer to the GHz to THz range (i.e., 1/ns to 1/ps), the conductivity of the interlayer might start to play a non-negligible role. At these frequencies, the contribution of the interlayer can be described by the frequency-dependent conductivity reported in the Supporting Information for the models tested.

3.1.2. Pore size dependence of the electrical conductivity and impedance

The correlation functions $\Phi_{T,\parallel}$ for the interlayer distances studied are presented in Fig. 3. The amplitude of oscillations is more pronounced for smaller d, with the correlated portions being higher and the anti-correlated portions deeper. The oscillations are damped on the picosecond timescale.

DC conductivity. DC conductivity of the confined electrolyte $\sigma^E(f = 0, d)$ is shown to decrease with increasing interlayer distance in Fig. 4(A). To compute $\sigma^E(f = 0, d)$, Eqs. (9)–(11) are used with the volume being the Voronoï volume of the confined electrolyte (whose dependence on the interlayer distance is reported in the Supporting Information). The xx, yy and zz components are similar. The DC conductivity of microporous C–S–H is calculated accounting for the volume of the electrolyte and that of the solid layers. The parallel component of the DC conductivity of microporous C–S–H $\sigma_\parallel(f = 0, d)$ is plotted in Fig. 4(B) as a function of the interlayer distance, d. The perpendicular component ($\perp$) is zero when the solid layers are considered insulators. Regarding the parallel component, the overall behavior indicates a plateau in $\sigma_\parallel(f = 0, d)$ with increasing d up to approximately 2–3 nm, followed by a decrease as d continues to grow. This result can be understood as the outcome of two competing effects:

- *Reduction in confinement*: As d increases, ion dynamics become less constrained, leading to higher mobility and, consequently, greater conductivity.
- *Reduction in ion concentration*: With increasing d, the total ion content remains constant, resulting in a lower ion concentration, which reduces conductivity.

The first effect is compensated by the second in micropores, while the second prevails in mesopores. In mesopores ($d >$ 2–3 nm), $\sigma_\parallel(f = 0, d)$ decreases with d as reduced ion concentration becomes the dominant factor. The loss of confinement is primarily observed in micropores, as indicated by the average Voronoï volume of ions, which increases with d up to 2–3 nm and then remains approximately constant for larger d (as shown in Fig. S1 (bottom) in the Supporting Information).

The parallel component of DC conductivity of C–S–H is fitted using:

$$\sigma_\parallel(f = 0, d) = A \frac{\exp\left[-\left(\frac{d}{B}\right)^C\right]}{d} \tag{27}$$

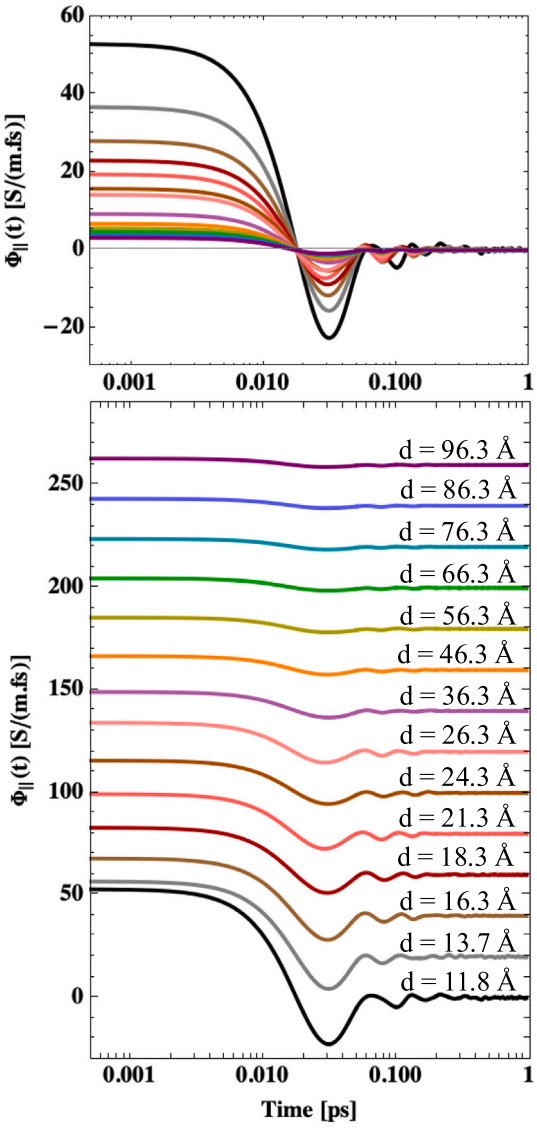

Fig. 3. Correlation functions $\Phi_{T,\parallel}$ as aa function of the time for the interlayer distances studied. The bottom figure shows the $\Phi_{T,\parallel}$ shifted upwards of 20 S/(m fs) for better visualization.

The fitting parameters are A = 87.54 ± 7.79 S/m, B = 14.58 ± 1.71 Å and C = 1.55 ± 0.41, with the coefficient of determination of the fitting being R^2 = 0.93. The expression above is used in upscaling the DC electrical conductivity of C–S–H gel in next section.

The response of the non-confined electrolyte with the same composition as the nanopore systems is presented in Fig. 4(C). The results are plotted as a function of the interlayer distance from which the composition was taken, allowing comparison of the different conductivities and the estimation of the interfacial contribution. As expected for non-confined systems, the conductivity is approximately isotropic. It exhibits a non-monotonous trend, with a maximum observed for systems corresponding to interlayer distances in the 2–3 nm range. This behavior can also be explained by the competing effects of reduced ion confinement and decreased ion concentration discussed above. The key difference here is that the reduction in ion confinement occurs locally due to the formation of a crowded ion cloud in smaller systems with higher ion concentration. The formation of contact ion pairs and the resulting ion–ion correlations are expected to reduce ion mobility, particularly in systems with interlayer distances in the 2–3 nm range.

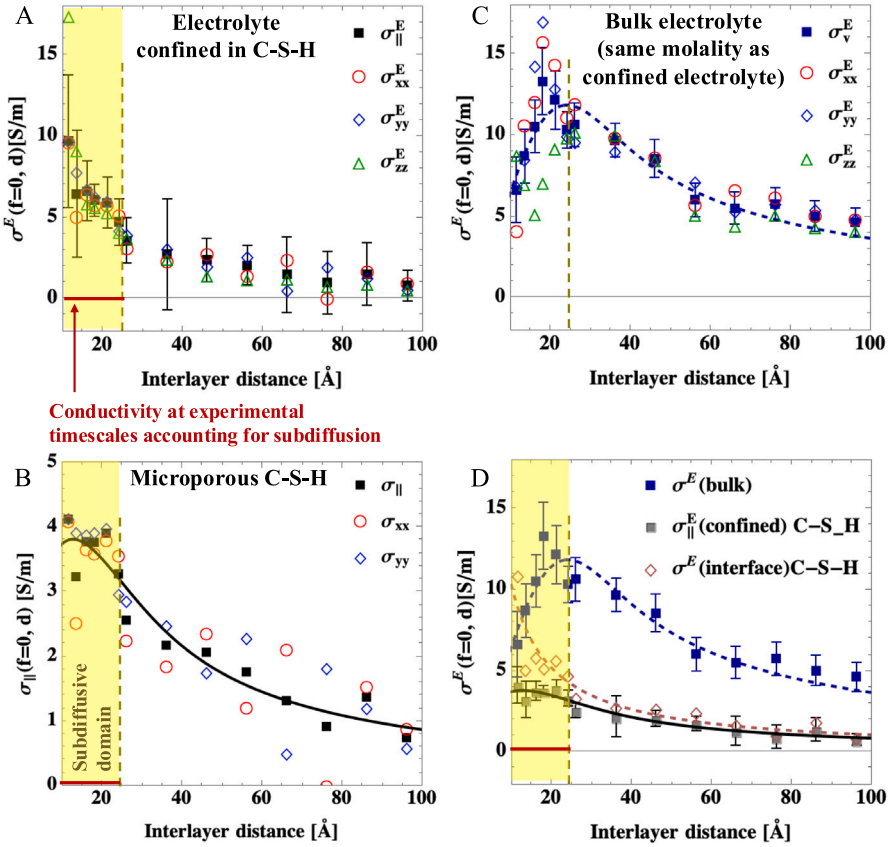

Fig. 4. DC conductivity of (A) the confined electrolyte $\sigma^E(0)$, (B) microporous C–S–H $\sigma_{\parallel}(0)$, and (C) bulk electrolyte with the same composition as the confined electrolyte. The xx, yy and zz components are shown for $\sigma^E(0)$. The xx and yy components are shown for $\sigma_{\parallel}(0)$ (the zz is zero when one consider the solid layers as insulators). (D) Comparison of the DC conductivity of the confined electrolyte, microporous C–S–H, and C–S–H interface (from Eq. (17)). (For interpretation of the references to color in this figure legend, the reader is referred to the web version of this article.)

The DC conductivity of the non-confined electrolyte is higher than that of the confined electrolyte, as expected for systems such as C–S–H, where hydrophilic, charged surfaces constrain the electrolyte. Confinement thus leads to a reduction in electrolyte conductivity. These results will be used in Section 3.2.3 to propose a strategy for accounting for the effects of the pore solution in cement systems, which is charged with additional ionic species that can further influence C–S–H gel conductivity.

The interface contribution, calculated using Eq. (17), is shown in Fig. 4(D), in a comparison with the DC conductivity of the confined electrolyte in C–S–H and that of microporous C–S–H. The interface contribution is similar to that of the confined electrolyte in the mesopore range, but it exceeds that of the confined electrolyte in the micropore range. In smaller systems, where a larger portion of the pore exists within the interfacial regime, the contribution and interaction with the solid surfaces are expected to play a more prominent role.

Finally, following the discussion from the previous section, it is important to note that subdiffusion may lead to a decrease in the DC conductivity values observed for micropores in Fig. 4. For this reason, we clearly identify the yellow zone corresponding to the subdiffusive domain. In this domain, the conductivity at experimental timescales — accounting for subdiffusion — can be considered close to zero. This effect should become less pronounced as Fickian diffusion begins to dominate over subdiffusive behavior with increasing pore size. One way to quantify how the transition from subdiffusion to Fickian diffusion affects the DC conductivity is to use the Nernst–Einstein expression coupled with generalized diffusion theory. To do so, one would need the evolution of D_α and α in Eq. (18) as a function of d. These calculations have not yet been reported in the literature and will be the subject of future work [49]. For the purposes of the upscaling approach proposed hereafter, the current understanding of the behavior at the basal spacing in the microporous range, as well as that across the various mesopore sizes, is sufficient. As for the micropore range, a more detailed analysis will focus on the pore size of d = 13.7 Å (basal distance for Kunhi et al. [32] model) pore size.

Frequency-dependent complex conductivity. Fig. 5 shows the real and imaginary parts of the frequency-dependent complex conductivity of C–S–H for different interlayer distances d, along with the contributions from the interface and the corresponding bulk electrolyte. Frequencies up to the THz range are considered to better visualize changes in conductivity. However, it should be noted that at such high frequency range, electron-level phenomena may occur, which cannot be accounted for using the classical simulations employed here. No changes in either term are observed up to the 10 GHz frequency range. Beyond this range, the real part exhibits an increasing trend, while the imaginary part shows a decreasing trend with the increasing frequency. This results is consistent with literature reports of constant conductivity at low frequencies and a power-law increase at high frequencies [55]. These changes occur at lower frequencies as the interlayer distance decreases. A non-monotonic response is observed in the real part of the conductivity for interlayer distances of 11.8 and 13.7 Å. However, this feature appears near the THz band, which may not be fully captured by the classical techniques used in this study.

For the *bulk electrolyte conductivity*, the real part increases above 100 GHz for $d > 30$ Å, while smaller d values display non-monotonic behavior with distinct maxima or minima. The imaginary part is stable up to 10–100 GHz, then decreases for all d, with the onset frequency again lower for smaller pores. The *interface conductivity*, calculated assuming additive impedances, shows a stable real part up to 100 GHz,

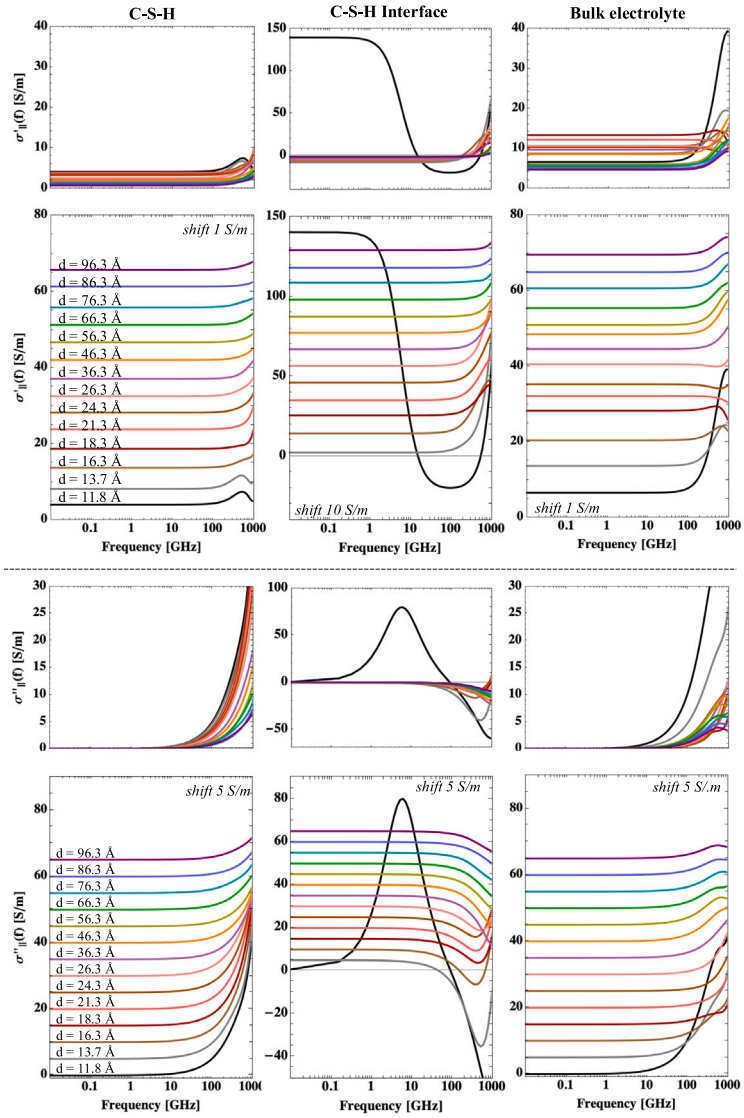

Fig. 5. Real $\sigma'_{\parallel}(f)$ and imaginary $\sigma''_{\parallel}(f)$ parts of the complex conductivity as a function of frequency for various interlayer distances d in C–S–H (left), for the interface (center) and the equivalent bulk electrolyte (right). For better visualization, the bottom figures display the results from the top figure shifted upwards (with the shift value noted in the figure) with increasing pore sizes. Note that, for better visualization, the scales of y-axis for the interface case are different from C–S–H and bulk electrolyte.

followed by a general increase. The smallest system (d = 11.8 Å) again shows a distinct non-monotonic pattern. The imaginary part is stable up to 10–100 GHz, then increases, often non-monotonically, with the onset frequency decreasing as d decreases.

Overall, confinement of the electrolyte in C–S–H reduces the real part of the conductivity at low to intermediate frequencies (≤100 GHz) and promotes a smoother, monotonic imaginary-part response. The shift of the imaginary-part decrease or increase onset to lower frequencies with decreasing d appears more related to electrolyte concentration than to confinement itself. The smallest pores display distinct behaviors, suggesting significant changes in ion transport/local relaxation mechanisms.

Impedance. Fig. 6 shows the complex impedance as a function of frequency for various interlayer distances d in C–S–H (left), for the interface (center), and for the equivalent bulk electrolyte (right). For the real part, the impedance remains constant up to a frequency in the 10–100 GHz range. The real part of the C–S–H impedance is overall significantly larger than that of the bulk electrolyte and slightly larger than that of the interface. The imaginary part is generally monotonic, with a maximum occurring within the 10–100 GHz range. In the micropore and small mesopore ranges, the peak position shifts slightly to higher frequencies with increasing pore size. However, the largest pore sizes tested show deviations from these trends.

Nyquist plots. Fig. 7 shows the Nyquist diagrams for the complex conductivity and impedance of the electrolyte confined in C–S–H for various pore sizes. The characteristic semi-circle or arc shapes are observed in almost all cases. However, deviations from this shape are noted for conductivity in small pore sizes. The oscillatory behavior for d = 11.8 and 13.7 Å might be due to the multiplicity of relaxation phenomena.

To aid in interpretation and provide a means of upscaling the pore size dependence of electrical conductivity, the Nyquist diagrams are fitted using two approaches: (i) relaxation models and (ii) equivalent circuits, as detailed below.

(i) Relaxation models. Two relaxation models are tested as detailed below.

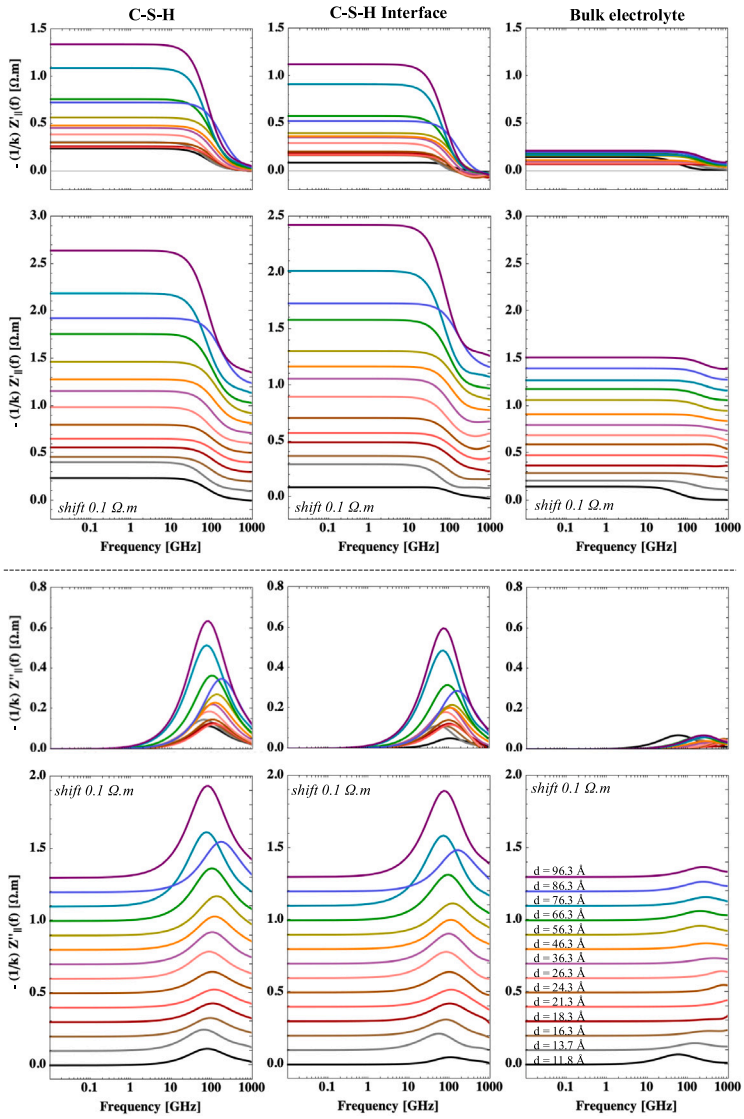

Fig. 6. Real $Z'_{\parallel}(f)$ and imaginary $Z''_{\parallel}(f)$ parts of the complex impedance as a function of frequency for various interlayer distances d in C–S–H (left), for the interface (center) and the equivalent bulk electrolyte (right). For better visualization, the bottom figures display the results from the top figure shifted upwards (with the shift value noted in the figure) with increasing pore sizes.

- **Jonscher's Universal Power Law**, adapted for ionic conducting or disordered systems [56], which we write for convenience as:

$$\sigma^{Jo}(f) = \sigma_0 + \left(2\pi i \frac{f}{f_c^{Jo}}\right)^{s^{Jo}} \tag{28}$$

where f_c^{Jo} is a material-dependent constant homogeneous to a frequency, and s^{Jo} is an exponent typically in the 0.5–1.0 range. This model can capture both dipolar response and carrier polarization phenomena in electrolytes or disordered solids [55–57], making it particularly interesting for evaluating the behavior of electrolytes confined in C–S–H, which exhibit a liquid-to-glass transition with increasing confinement [16,18].

- **Havriliak–Negami Model** [58]:

$$\sigma(f) = \sigma_\infty^{HM} + \frac{\sigma_0 - \sigma_\infty^{HM}}{[1 + (i2\pi f \tau^{HM})^{1-\alpha^{HM}}]^{\beta^{HM}}} \tag{29}$$

where σ_0 and σ_∞^{HM}, associated with the DC conductivity and high-frequency limit conductivity, respectively; τ^{HM} is the relaxation time; α^{HM} controls the width of the relaxation spectrum; and β^{HM} allows for additional skewing of the relaxation. This model generalizes the Cole-Cole model (where $\beta^{HM} = 1$), which in turn generalizes Debye model (where $\beta^{HM} = 1, \alpha^{HM} = 0$). The Cole-Cole model has been used to fit the dielectric behavior observed in molecular simulations of pore solutions in cement systems [59] and water confined in C–S–H [20].

(ii) Equivalent circuits. The circuits in Fig. 8 were tested, and the one with two ideal parallel RC elements in series provided the best results when all interlayer distances, including both micro- and mesopore ranges, were accounted for. Each branch produces a perfect semicircle in the Nyquist plot (without depression, since they are ideal RCs). Factors such as surface roughness, extreme confinement, and interfacial contributions are known to induce non-uniformity in relaxation processes, resulting in a distribution of relaxation times. In such cases, the use of non-ideal elements may be relevant. A constant phase element (CPE) is typically employed, with impedance $Z_{CPE} = Q(j2\pi)^{\psi}$, where Q is the pseudo-capacitance, and the exponent ψ (with $0 < \psi \leq 1$), with $\psi = 1$ being a pure capacitor behavior, $\psi = 0$ being a pure resistor behavior, and intermediary values corresponding to "imperfect capacitor"/non-ideal RC. CPE has also been used to interpret subdiffusive dynamics [60]. Fits using CPEs were applied to capture micropore

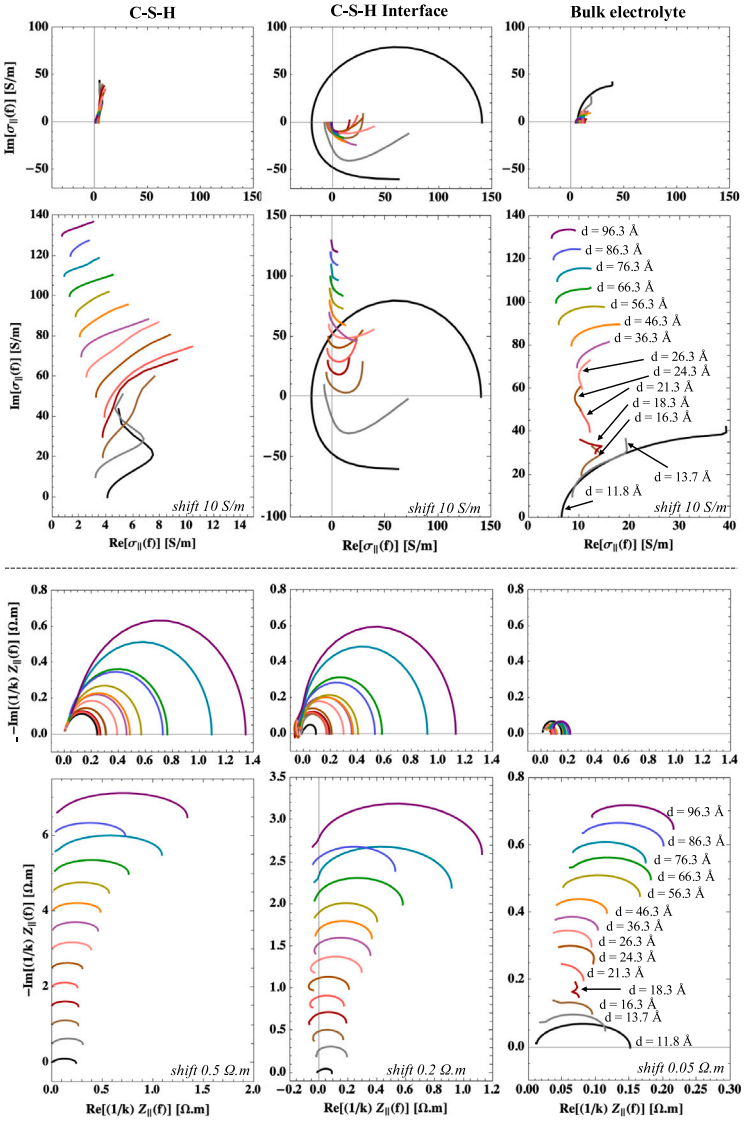

Fig. 7. Nyquist diagram of the complex conductivity (top) and impedance (bottom) and Debye models (since Jonscher's Universal Power Law for various interlayer distances d in C–S–H (left), for the interface (center) and the equivalent bulk electrolyte (right). For better visualization, the bottom figures display the results from the top figure shifted upwards (with the shift value noted in the figure) with increasing pore sizes.

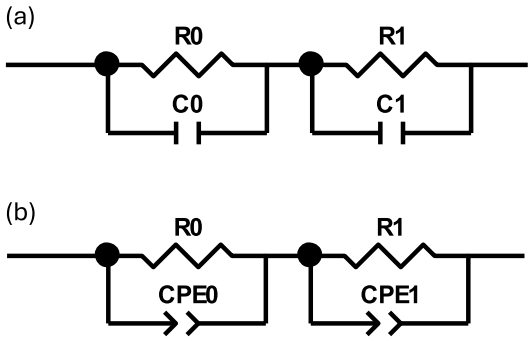

Fig. 8. Equivalent circuits tested: (a) 2RC circuit and (b) 2RC with constant phase element (CPE).

behavior but resulted in non-physical values of ψ. For this reason, they are not further explored in this study.

- **2RC Equivalent circuit** The expression for the retained equivalent circuit is given below. The real and imaginary parts of the impedance read, respectively:

$$(1/k)\cdot Z'(f,d) = \frac{R_0}{1+\left(R_0C_0(2\pi f)\right)^2} + \frac{R_1}{1+\left(R_1C_1(2\pi f)\right)^2} \tag{30}$$

$$(1/k)\cdot Z''(f,d) = -\left(\frac{R_0^2C_0(2\pi f)}{1+\left(R_0C_0(2\pi f)\right)^2} + \frac{R_1^2C_1(2\pi f)}{1+\left(R_1C_1(2\pi f)\right)^2}\right) \tag{31}$$

where the resistors and capacitor values are a function of the interlayer distance following the fittings (for d in Å):

$$R_0(d) = 0.0063\cdot e^{0.0222d} \tag{32}$$

$$R_1(d) = 0.1968\cdot e^{0.0187d} \tag{33}$$

$$C_0(d) = 2.1\times10^{-9}\cdot d^{-1.904} \tag{34}$$

$$C_1(d) = 8.5\times10^{-11}\cdot d^{-0.893} \tag{35}$$

The ideal RC relaxations associated with each RC is given by $\tau_i = R_i C_i$. This relaxation time grows for both R_0C_0 and R_1C_1 grow with confinement, being consistent with the relaxation time reported for dielectric process in C–S–H [20]. The relaxation time of R_1C_1 also slightly grows for d above 60 Å which might be related to fitting uncertainties. The relaxation times for R_0C_0 element is similar to the one obtained for Havriliak–Negami Model in the 0.1 ps scale; the relaxation times for R_1C_1 is on the 1 ps scale.

Details on how the fits are performed and the fitting quality are provided in the Supporting Information. The fitting with the relaxation models captures the general behavior of the Nyquist plots. The fits obtained with models containing a larger number of fitting parameters naturally provide better agreement with the individual values associated with a given interlayer distance. When the general trends as a function of d are adopted for the fitting parameters, a decrease in the coefficient of determination is observed for small d, accompanied by large associated errors, as calculated in the Supporting Information. The oscillatory features of the conductivity for systems at d = 11.8 and 13.7 Å in the Nyquist plots are not accurately captured with the proposed models, but provide a fair approximative description of the behavior in these small pores. The equivalent circuit and relaxation models yield good fittings for mesopores, with similar fitting quality. Hereafter, the equivalent circuit is retained for the upscaling of conductivity, since it is a framework that the experimental community is more accustomed to when interpreting impedance/complex conductivity results.

3.2. Gel scale

The effective properties of C–S–H gel are estimated using the multiscale strategy outlined described in Section 2.5, accounting for different gel pore sizes. The effective pore size d_{eff} in C–S–H is expressed as a function of the interlayer spacing d, based on the Voronoï volume of interlayer species (see Supporting Information A) and a C–S–H surface area (here, 490 Å^2 in the xy plan for the systems simulated):

$$d_{eff} \approx 0.97d - 6.7 \tag{36}$$

with d in Å. Herein, the gel pore size is then approximated as $d_g \approx d_{eff}$.

3.2.1. DC conductivity

For the application of the Eq. (24), the behavior of the microporous solid and of the gel needs to be defined. The conductivity of *microporous C–S–H* has been discussed earlier for various timescales and two options can be considered for the conductivity associated with microporous C–S–H:

- The conductivity associated with the experimental testing timescale, on the order of seconds, $\sigma^s_{\|,s} = 4.53 \times 10^{-11}$ S/m (Table 2).
- The conductivity associated with the timescale corresponding to the characteristic size of C–S–H particles (stacked domains), denoted as $\sigma^p_{\|,s}$. C–S–H particles are on the order of a few nanometers [31,61], and the associated timescale to traverse this length can be estimated as [51] $t_{1nm} = (10^2/D_\alpha)^{1/\alpha}$. In this context, the corresponding timescales for interlayer OH and Ca are on the order of 10 μs and several years, respectively, using the data from Table 3 for Kunhi et al. [32] C–S–H modeled with ClayFF. The value 10 μs for OH must control response because it leads to conductivity in experimentally accessible timescales. The associated conductivity (see Eq. (37) and associated discussion in the next section) is of 10^{-6} to 10^{-5} S/m.

Table 4
Effective conductivity of the C–S–H gel for packing densities associated with high-density (HD) and low-density (LD). The pore solution conductivities at early age (EA) and late ages (LA) are taken as σ_{PS} = 3 S/m and σ_{PS} = 10 S/m according to typical values reported for ordinary cement systems [13].

	d_g [nm]	σ [S/m]	σ/σ_{PS} (EA) [–]	σ/σ_{PS} (LA) [–]	ρ [Ω.m]
LD	2 (Iso)	0.118	0.0392	0.0118	8.50
	2 (2D)	3.86E−5	1.28E−5	3.86E−6	2.59E4
	5 (Iso)	0.0658	0.0219	6.58E−3	15.2
	5 (2D)	3.86E−5	1.28E−5	3.86E−6	2.59E4
	10 (Iso)	0.0251	8.37E−3	2.51E−3	39.8
	10 (2D)	3.86E−5	1.28E−5	3.86E−6	2.59E4
HD	2 (Iso)	9.23E−5	3.10E−5	9.23E−6	1.07E4
	2 (2D)	2.62E−5	8.72E−6	2.62E−6	3.82E4
	5 (Iso)	9.23E−5	3.10E−5	9.23E−6	1.07E4
	5 (2D)	2.62E−5	8.72E−6	2.62E−6	3.82E4
	10 (Iso)	9.23E−5	3.10E−5	9.23E−6	1.07E4
	10 (2D)	2.62E−5	8.72E−6	2.62E−6	3.82E4

We consider that the second case is more appropriate because it accounts for the microstructure of C–S–H and the related time/length scales. A value of $\sigma^p_{\|,s} = 10^{-5}$ S/m is adopted herein. Due to the percolative behavior discussed later, adopting $\sigma^s_{\|,s} = 4.53 \times 10^{-11}$ S/m instead would have a negligible effect on the conductivities below the percolation threshold η (while the estimates above the percolation threshold should be on the order of $\sigma_{\|,s}$.)

For the *gel pores*, estimates assuming isotropic and 2D behavior are considered, following the discussion of a previous study on dielectric permittivity [20]. For dielectric permittivity, it was shown that dimensionality suppression might persist for pore sizes above the tens-of-nanometer scale [62]. The idea of testing both 2D and isotropic behavior here is to evaluate which choice is better suited to describe conductivity in C–S–H.

The effective DC conductivity of C–S–H gel is shown in Fig. 9(A) as a function of C–S–H packing density. In both 2D and isotropic cases, the behavior shows percolative characteristics, with the effective response being conductive for packing densities below η_c and insulative for packing densities above this value. The associated percolation threshold, defined as the minimum volume fraction of the conductive phase for the effective behavior to be conductive, is $f_c = 1 - \eta_c$. For random materials with one conductive phase and one insulating phase with polycrystalline morphology and spherical inclusions, the percolation threshold is $f_c^{spheres} = 1/3$ (i.e., $\eta_c = 2/3$) [2]. Consistently with this values, in the case of isotropic gel pores, we obtained a percolation threshold at $\eta_c = 2/3$. For packing densities below this value, the system is conductive and dominated by mesopores, whereas for densities above this threshold, it becomes insulating and dominated by the microporous solid. On the other hand, the percolation threshold obtained for the case with 2D behavior of the gel pores being below than $\eta_c = 2/3$ indicates that decreasing the dimensionality of conductivity (by suppressing the conductivity perpendicular to the C–S–H layer for interlayers and also for gel pore in the 2D case) leads to an decrease in the values of η_c. The DC conductivities for packing densities above the percolation value are, as discussed above, on the order of $\sigma_{\|,s}$.

The effective resistivity of C–S–H gel is shown in Fig. 9(B) as a function of C–S–H packing density. The percolative features are also reflected in the resistivity, with the resistivities for packing densities above the percolation threshhold being of $1/\sigma_{\|,s}$.

The corresponding values for packing densities of 0.64 and 0.74 are reported in Table 4. These packing densities are associated with low-density (LD) and high-density (HD) C–S–H [63], respectively, and can be readily used in multiscale modeling. It should be noted that above the percolation threshold, the microporous phase dominates, and the estimates become essentially identical for the different pore sizes tested (differences only appear beyond the fourth or fifth significant figure).

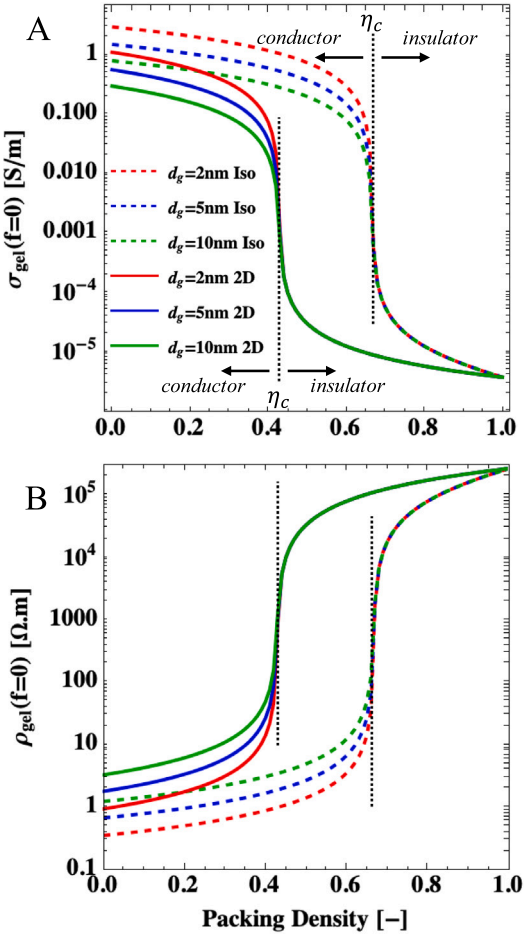

Fig. 9. Effective DC (A) conductivity and (B) resistivity of C–S–H gel as a function of the packing density following the microstructure representation and multiscale strategy outlined in Fig. 1. Three gel pore sizes (d_g = 2, 5 and 10 nm) are considered with a 2D or isotropic behavior being adopted for the gel porosity.

This is the case for LD with d_g of 2, 5, and 10 nm for the 2D case, as well as for all 2D values or the isotropic value for HD. These values in Table 4 can be compared with conductivities that have been associated with C–S–H (or hydrates more generally) in the literature. For example, a DC conductivity of 0.0246 ± 0.0384 S/m has been reported for the solid phase in cement pastes [2]. In addition, several authors report the conductivity of C–S–H (σ) relative to the conductivity of the pore solution (σ_{PS}): σ/σ_{PS} (i.e., a formation factor-like parameter) equal to 1/400 = 0.0025 [3], 1/300 = 0.00333 [4], 1/129 = 0.00775 [5], and 1/121 = 0.00826 [6]. For comparison with these results, we consider in Table 4 typical values of pore solution conductivity in ordinary cement system associated with early age (σ_{PS} = 3 S/m) and late ages (σ_{PS} = 10 S/m) [13]. Our results for the LD cases with isotropic behavior for gel pores are in good agreement with most of the reported data.

Additionally, the results in Fig. 9 can be used to estimate the DC conductivity response of C–S–H upon densification, which might occur due to an increase in the number of layers in the stacked domain and a possible transitioning from the growth of a low-density product containing gel pores to a higher-density product with lower gel pores content [64]. This aspect is a valuable input for multiscale modeling [65,66], in particular at early-age, and is yet to be fully accounted for in the study of transport and electromagnetic properties of cement systems.

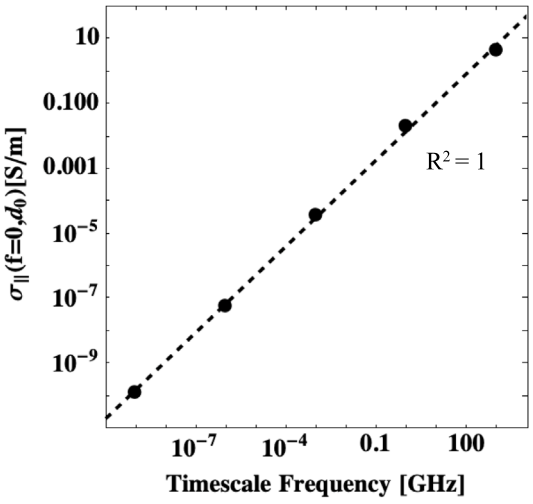

Fig. 10. Frequency-dependence of the DC conductivity of C–S–H at the basal spacing: symbols are the Nernst–Einstein DC conductivity (from Table 2 using Kunhi et al. [32] C–S–H with ClayFF); the dashed line is a fit with Eq. (37) for which the determination coefficient is reported.

3.2.2. Frequency-dependent response

The discussion in Section 3.1.1 highlights the need to consider frequency dependency in the response of the system at basal spacing (microporous C–S–H): the response at the second timescale is effectively that of an insulator, while at the timescale associated with the THz range, the conductivity reaches values on the order of S/m, representing a difference of several orders of magnitude. The results in Table 2 provide a way to quantify this effect, with the corresponding values plotted in Fig. 10 (top). The following power law fits this trend

$$\sigma_{\parallel,s}(f_\tau, d_0) = 0.0158 f_\tau^{0.8877} \tag{37}$$

for $f_\tau = 1/\tau$ in GHz and τ being the timescale considered in the evaluation of the conductivity. We can use this relation to write a frequency-corrected expression for the conductivity of C–S–H at the basal spacing assuming that the complex conductivity is modulated by the DC conductivity following a given relaxation or equivalent circuit model for the corresponding pore size:

$$\sigma^c_{\parallel,s}(f, d_0) = c_f(f)\sigma^{CE,c}(f, d_0) \tag{38}$$

where $c_f(f) = (0.0158 f^{0.8877}/\sigma_{\parallel,s}(f_\tau = 1000, d_0)) + \sigma^p_{\parallel,s}$ (for f in GHz) is the frequency correction factor (where $\sigma^p_{\parallel,s}$ was added to so that the minimum conductivity at low f can be reproduced and the corresponding impedance can be calculated, avoiding division by zero), and the basal spacing is d_0 = 13.7 Å following Kunhi et al. [32] model. Herein, we adopt the $\sigma^{CE,c}(f, d_0)$ for the equivalent circuit discussed in the previous sections. With the expression above the behavior at the THz scale is identical to that reported in Fig. 10 for d = 13.7 Å, and that at the Hz scale corresponds to an effective insulator.

The estimated frequency-dependent response of the C–S–H gel is shown in Fig. 11. The real and imaginary parts of the conductivity decrease with increasing η for d_g = 2 nm. For d_g = 5 and 10 nm, this trend is inverted above frequencies in the GHz–THz range. The Nyquist plots of the conductivity display arcs with decreasing curvature as η increases and appear nearly linear within the studied frequency range for the largest packing densities.

Regarding the impedance, the real and imaginary components increase with η for a given f. The peak of the imaginary component moves toward lower frequencies with increasing η. For low η, the Nyquist diagrams yield nearly ideal semicircles of smaller radius, typical of Debye-type relaxation. As η increases, the left side of the semicircle becomes progressively deformed, and the arcs fail to close

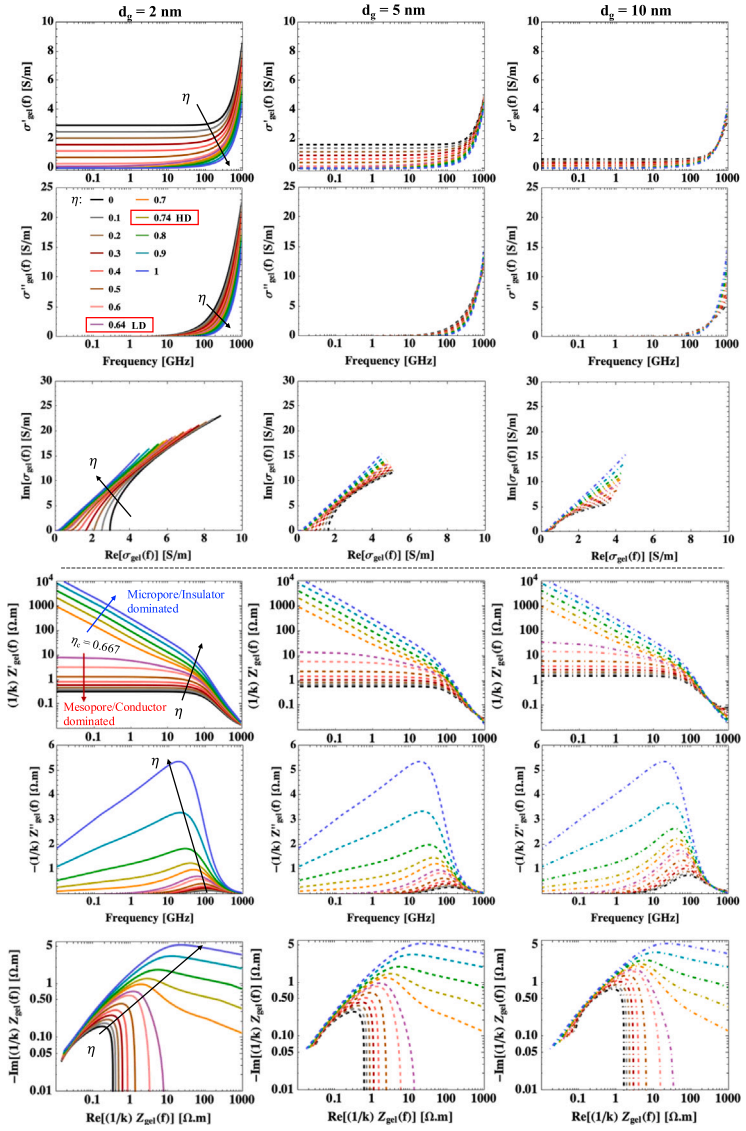

Fig. 11. Frequency-dependent response of the C–S–H gel considering various packing densities η and three gel pore sizes are considered d_g = 2, 5 and 10 nm. The isotropic behavior for the gel porosity is adopted. The equivalent circuit model is adopted to fit the behavior at the molecular scale and the correction proposed in Eq. (38) is accounted for (see the Supporting Information F for the estimates where the correction is not accounted for). Log-Log plots are adopted for the Nyquist plots of impedance for better visualization. (For interpretation of the references to color in this figure legend, the reader is referred to the web version of this article.)

on the real axis, leaving a persistent non-zero imaginary contribution at high real values. The transition of closing arc to non-closing arc with persistent tails at large real impedance occurs at the percolation threshold. This behavior illustrates the effective impedance response of C–S–H when micro- and mesopores coexist. Systems with 100% mesopores (η = 0, black curve) produce a nearly perfect semicircle, reflecting a well-defined single relaxation time. In contrast, systems with 100% micropores (η = 1, dark blue curve) generate strongly distorted arcs, consistent with a broad distribution of relaxation times and long-lived polarization effects induced by nanoscale confinement. Intermediate cases, corresponding to mixed pore structures, show a gradual deformation from the ideal semicircle toward elongated, non-closing arcs. These results highlight that increasing packing density, i.e., the fraction of micropores, enhances confinement effects, introduces additional relaxation mechanisms, and leads to heterogeneous impedance behavior governed by a wide distribution of relaxation times. This distortion in the arcs with larger microporous content does not appear when the correction in Eq. (38) is omitted (see Supporting Information F for the effective electrical response without the frequency correction). Experimental confirmation of the persistent right tails in the Nyquist plots of the impedance is required, ideally through measurements on synthesized C–S–H or on materials with a high C–S–H content, such as C_3S pastes.

The results for LD and HD C–S–H are reported in Fig. 12. LD and HD C–S–H exhibit distinct behaviors. Since LD is below the percolation threshold η_c, it shows closing arcs in the Nyquist diagrams of the impedance. In contrast, HD displays a persistent right-hand tail. The relaxation models and equivalent circuits presented in Section 3.1.2 are not suitable for reproducing these persistent tails. Better-suited models need to be developed to fit the behavior of C–S–H gel in this context. These results suggest that, upon densification, C–S–H may exhibit a change in impedance behavior when the percolation threshold is reached.

3.2.3. Accounting for ions in the pore solution of cement system

The pore solution in cement systems is charged with alkali and hydroxide ions (high pH), as well as calcium, sulfate, and minor species [67]. Some of these ions can be present in the gel porosity,

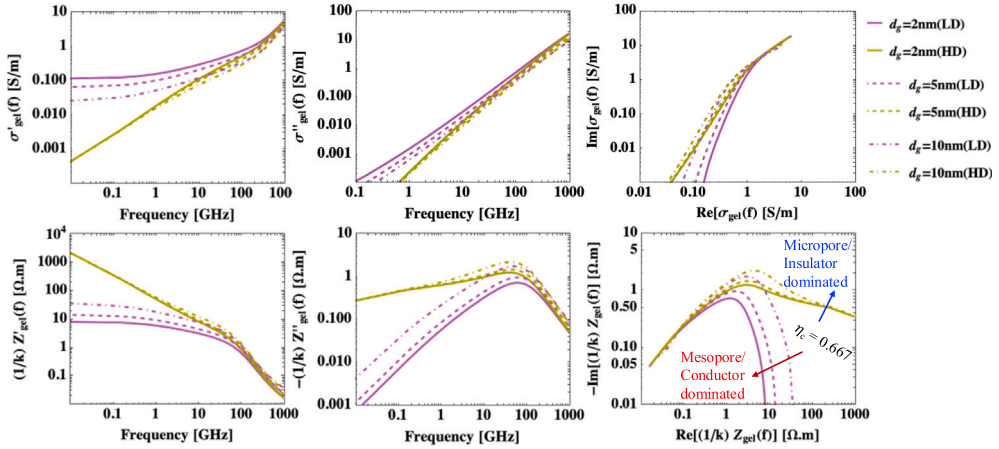

Fig. 12. Frequency-dependent response of the HD and LD C–S–H gel considering three gel pore sizes (d_g = 2, 5 and 10 nm). The isotropic behavior for the gel porosity is adopted. The equivalent circuit model is adopted to fit the behavior at the molecular scale and the correction proposed in Eq. (38) is accounted for. Log-Log plots are adopted for the Nyquist plots of impedance for better visualization.

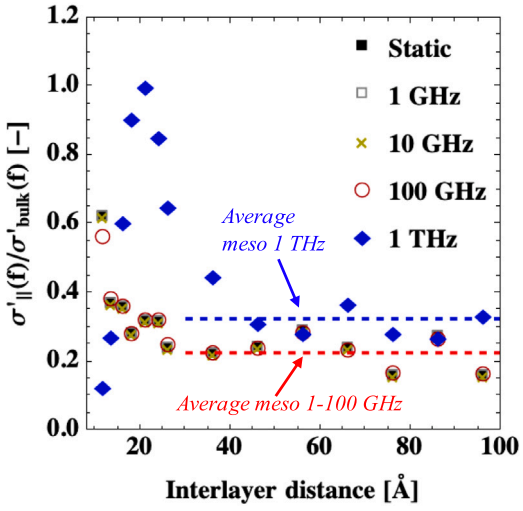

Fig. 13. Frequency dependent formation factor: ratio between the conductivity of C–S–H and that of the non-confined electrolyte (with the same composition as the electrolyte confined in C–S–H) as a function of the interlayer distance for various frequencies. The average values for all interlayer distance in the mesopore range (above 3 nm) are provide. The values for frequencies 0–100 GHz superpose.

thereby affecting the overall electrical conductivity of C–S–H. In this section, we propose a simplified approach to account for these effects.

As discussed in Section 3.1.2, confinement in C–S–H reduces the conductivity of an electrolyte. Fig. 13 presents the ratio between the GK conductivity of C–S–H and that of the non-confined electrolyte (with the same composition as the confined electrolyte) $\sigma'_{\parallel}(f)/\sigma'_{\text{bulk}}(f)$ as a function of interlayer distance for various frequencies. This factor resembles the definition of a formation factor, but accounts for measurements at finite frequencies (i.e., $f \neq 0$). A decreasing trend is observed when $\sigma'_{\parallel}(f)/\sigma'_{\text{bulk}}(f)$ is plotted against interlayer distance in the 0–100 GHz range. At the THz scale, however, a non-monotonic trend appears, with a maximum around $d \approx 20$ Å. For all frequency ranges, $\sigma'_{\parallel}(f)/\sigma'_{\text{bulk}}(f)$ approximately saturates in the mesopore range (above 3 nm). The average values across all interlayer distances in this range are reported. For 0–100 GHz, the values converge to an average of $\sigma'_{\parallel}(f)/\sigma'_{\text{bulk}}(f)$, while at the THz scale the average value is slightly higher, $\sigma'_{\parallel}(f)/\sigma'_{\text{bulk}}(f) = 0.326$.

The concentration of the pore solution is typically moderate, generally not exceeding 1 mol/L at late ages, although variability exists depending on the type of cement used [67]. Due to ion exclusion effects as well as electrostatic and steric repulsion, the same concentration as in larger pores may not be attainable in interlayer pores. This aspect still requires detailed study. Because of their larger size, mesopores in C–S–H gel are more likely to contain a pore solution composition similar to that found in the bulk pore solution. We therefore apply the correction factor $\sigma'_{\parallel}(f)/\sigma'_{\text{bulk}}(f) = 0.227$ (valid in the 0–100 GHz range) to account for the effect of the pore solution on mesopore only for the estimation of the conductivity of C–S–H. Using this factor, and adopting typical pore solution conductivities in ordinary cement systems as in Table 4: $\sigma_{PS} = 3$ S/m at early ages and $\sigma_{PS} = 10$ S/m at late ages; we estimate an increment in conductivity of $\delta\sigma = \sigma'_{\parallel}(f)/\sigma'_{\text{bulk}}(f) \times \sigma_{PS} \approx 0.7$ S/m for early ages and ≈ 3 S/m for late ages. Incorporating these increments into the DC conductivity estimates of C–S–H, and assuming isotropic behavior of the gel pores, we obtain the values reported in Table 5. The resulting conductivities are of the same order of magnitude as those reported in Table 4. By extension, we can expect that the complex conductivity and impedance will also be of the same order of magnitude as the values reported previously without accounting for pore solution conductivity.

Both types of estimates — those accounting for pore solution conductivity and those not accounting for it — are relevant for understanding the behavior of C–S–H. The former corresponds to C–S–H in real cement systems, while the latter corresponds to "pure" or synthesized C–S–H. The present results therefore suggest that the conductivity of C–S–H in cement systems must exceed that of synthesized C–S–H by an increment of at least a fraction of a S/m.

4. Conclusions

Frequency-dependent complex conductivity and impedance of C–S–H at both the molecular and gel scales are estimated for the first time using a bottom-up multiscale approach combining molecular simulations with micromechanics homogenization. This enables a direct link between nanoscale ion dynamics and the effective electrical response of the C–S–H gel. The following conclusions can be drawn from this study:

- *1. DC ionic conductivity of C–S–H interlayers is extremely reduced by subdiffusion.* Across all calcium silicate hydrates tested, the subdiffusive dynamics of ions in the interlayer result in effective conductivities — on timescales above the microsecond — several orders of magnitude lower than the typical 1–10 S/m range of

Table 5
Effective conductivity of the C–S–H gel *accounting for cement-based materials pore solution* for packing densities associated with high-density (HD) and low-density (LD). The pore solution conductivities at early age (EA) and late ages (LA) are taken as σ_{PS} = 3 S/m and σ_{PS} = 10 S/m according to typical values reported for ordinary cement systems [13].

	Age	d_g [nm]	σ [S/m]	σ/σ_{PS} [–]	ρ [Ω.m]
LD	EA	2 (Iso)	0.146	0.0486	6.86
	EA	5 (Iso)	0.0872	0.0291	11.5
	EA	10 (Iso)	0.0591	0.0197	16.9
	LA	2 (Iso)	0.209	0.0209	4.78
	LA	5 (Iso)	0.151	0.0151	6.63
	LA	10 (Iso)	0.123	0.0123	8.15
HD	EA	2 (Iso)	2.44E−5	8.14E−6	4.09E4
	EA	5 (Iso)	2.44E−5	8.14E−6	4.09E4
	EA	10 (Iso)	2.44E−5	8.14E−6	4.09E4
	LA	2 (Iso)	2.44E−5	2.44E−6	4.09E4
	LA	5 (Iso)	2.44E−5	2.44E−6	4.09E4
	LA	10 (Iso)	2.44E−5	2.44E−6	4.09E4

bulk pore solutions. Thus, at the interlayer level, C–S–H behaves as an electrical insulator under DC conditions. Such reduced dynamics are not captured by Green–Kubo calculations, whose time integration is restricted to the picosecond scale, making them suitable only for Fickian diffusion or very high frequencies (hundreds of GHz). This insight is also relevant for other electrolyte-confined phases such as AFm, AFt, and ASR products.

- *2. Electrical conductivity of C–S–H is strongly anisotropic*. The dominant contribution to conductivity lies along the direction parallel to the interlayer plane, reflecting the slit-like confinement. This confirms that reduced dimensionality — previously noted for diffusion and dielectric permittivity — must also be considered when modeling conductivity at both interlayer and gel-pore scales.
- *3. DC conductivity of C–S–H shows marked pore-size dependence*. The parallel component of DC conductivity follows an exponential decay with decreasing interlayer spacing for systems at fixed ion concentration. Ionic conductivity results from two competing effects: (i) reduced confinement enhances ion mobility, while (ii) increased spacing lowers ion concentration. Consequently, confined electrolytes consistently show lower DC conductivity than bulk solutions of the same chemical composition.
- *4. Frequency-dependent conductivity at the molecular scale exhibits strong pore-size effects*. No significant variation occurs in either the real or imaginary components of complex conductivity up to 10 GHz, in agreement with literature showing constant low-frequency conductivity followed by a power-law increase. Consistent with DC trends, the real part of the complex conductivity is much lower than that of the corresponding bulk electrolyte, indicating that nanoscale confinement suppresses conductivity at low-intermediate frequencies (10–100 GHz) and produces a smoother imaginary-part response.
- *5. Relaxation and equivalent-circuit models capture the conductivity and impedance response of C–S–H*. Both Jonscher's UPL and the Havriliak–Negami model, together with the proposed equivalent circuit, provide a physically meaningful interpretation of the frequency-dependent behavior and can serve as inputs for multiscale modeling. While micropores exhibit more complex behavior, these models provide reasonable approximations.
- *6. Gel-scale electrical response can be obtained using a micromechanics approach*. DC conductivity estimates assuming isotropic gel pores agree with reported conductivity values for hydrates and C–S–H in the literature [2–6]. The results presented here constitute the first bottom-up estimate of the electrical response of C–S–H across scales. Effects of multicomponent pore-solution chemistry are quantified using a simplified model, and the trends offer guidance for further refinement, including explicit ion–surface coupling, ion-exclusion effects, and species relevant to durability.

In this study, we address the lack of quantitative, multiscale data on the frequency-dependent electrical conductivity of C–S–H, which remains a critical gap for interpreting electromagnetic measurements and for developing physics-based multiscale models of cementitious materials. To fill this gap, we quantify the electrical conductivity and impedance of C–S–H at both the molecular and gel scales by combining molecular simulations with mean-field homogenization. At the molecular scale, we assess the sensitivity of direct-current and frequency-dependent conductivities to the choice of force field and decompose the contributions of ion self-interactions, ion–ion interactions, ion–surface interactions, and ion–solvent interactions within an anisotropic framework consistent with the layered structure of C–S–H. The influence of nanoscale confinement is examined by comparing conductivities obtained in confined and non-confined electrolyte systems. At the gel scale, effective conductivities are computed using established homogenization formulations, and the predicted values are compared with available experimental data. Finally, we propose a correction to account for the influence of pore-solution ions in cement systems. This integrated approach provides the first comprehensive, multiscale characterization of the electrical response of C–S–H suitable for engineering applications.

An illustration of the applicability of the work is the use of the computed frequency-dependent electrical conductivity of C–S–H as input for multiscale transport and durability models, where reliable phase-level properties are required. The results also support the interpretation of impedance and resistivity measurements by clarifying how confinement and ion dynamics govern the electrical response of C–S–H. Thus, the proposed framework provides a practical link between molecular-scale mechanisms and measurable electrical properties in cementitious materials.

Research limitations. The present study focuses on model systems with simplified ionic compositions and does not explicitly account for the full multicomponent chemistry of pore solutions in cementitious materials. While the relaxation models used successfully capture the main features of the frequency-dependent response, they provide only approximate descriptions of the behavior of the smallest gel and interlayer pores. Additionally, the molecular simulations were performed for idealized slit-like geometries, and potential ion- or salt-exclusion effects in extremely confined pores were not explicitly modeled. These factors may slightly limit the direct transferability of some quantitative results to highly heterogeneous or chemically complex cement systems.

Recommendations for future research. Future work should extend the present multiscale framework to include realistic multicomponent ionic solutions representative of mature cement pore fluids, enabling a more complete description of conductivity and impedance in C–S–H. Detailed simulations of ion and salt exclusion in nanopores are also needed to clarify their influence on electrical properties, especially in the subnanometer confinement regime. Experimental studies targeting the persistent right-tail behavior in Nyquist plots would provide valuable validation of the proposed equivalent circuits and relaxation models. Finally, integrating the present bottom-up data into larger multiscale models may support improved interpretation of electromagnetic measurements and enhance predictive modeling of durability-related processes in cementitious materials. In particular, future work could build on these baseline results to develop multiscale models that explicitly incorporate aggregates and ITZ heterogeneity, enabling more accurate predictions of concrete's macroscopic electrical conductivity.

Table 6
List of symbols.

α	Anomalous diffusion exponent
α^{HM}, β^{HM}	Parameters that controls the width and additional skewing of the relaxation spectrum, respectively
c_j	Molar concentration of ion i
C_0, C_1	Capacitances of the two RC branches in the equivalent circuit
$c_f(f)$	Frequency correction factor applied to the DC conductivity.
d	Interlayer distance
d_{eff}	Pore thickness in the direction of the confinement
d_g	Gel pore size
D_α	Generalized (or fractional) self-diffusion coefficient
$\vec{E}$	Electric field
f	Applied frequency
f_c^{Jo}	Material-dependent characteristic frequency in Jonscher's model
$f_c^{spheres}$	Percolation threshold for systems with spherical conductive inclusions
f_τ	Characteristic frequency ($f_\tau = 1/\tau$), expressed in GHz.
i	Denotes the imaginary unit
f_g	Fraction that represents the gel porosity
$\vec{J}_I$, $\vec{J}_{I+}$, $\vec{J}_{I-}$	Contribution of ions to the cross-correlation of ion current, cations, and anions, respectively
k_B	Boltzmann constant
k	Geometric scaling factor applied to normalize the impedance
LD, HD	Low- and high-density C–S–H
$\vec{\mu}$	Dipolar moments
N	Number of atoms in the system
N_{ions}	Number of ions in the system
η_c	Percolation threshold for packing density
$\vec{P}$, $\vec{P}_W$, $\vec{P}_S$	Total, solvent and solid polarization
$\Phi_{AB,kl}$	General expression for the cross-correlation function of species A and B per direction kl
ψ	Exponent of the CPE, defining deviation from ideal capacitive behavior
Q	Pseudo-capacitance parameter of the CPE
$\vec{r}_i$	Position of atom i
$\langle r^2(t)\rangle$	Mean-squared displacement (MSD)
R_0, R_1	Resistances of the two RC branches in the equivalent circuit
σ_{PS}	Pore solution conductivity
σ'_{bulk}	Conductivity of the bulk electrolyte
σ', σ''	Real and imaginary component of frequency-dependent ionic conductivity
σ_{II}, σ_{IW}, σ_{IS}	Contribution of ion-ion, ion-solvent, ion-solid correlations to conductivity
σ^{hom}	Effective electrical conductivity of C–S–H gel
σ^{Jo}	Complex conductivity described by Jonscher's universal power-law model
σ_0	DC conductivity component
σ_∞^{HM}	High-frequency limit of the conductivity.
σ/σ_{PS}	Formation factor (conductivity ratio relative to pore solution).
$\sigma^c_{\parallel,s}(f,d_0)$	Frequency-corrected conductivity of basal-spacing C–S–H.
$\sigma^s_{\parallel,s}$	In-plane conductivity of the microporous C–S–H at experimental (seconds) timescale
$\sigma^p_{\parallel,s}$	In-plane conductivity of the microporous C–S–H at particle-scale (nanometer) timescale
$\sigma^{CE,c}(f,d_0)$	Conductivity obtained from the equivalent-circuit model for basal-spacing C–S–H.
$\sigma^{NE}_{t\to\tau}$	DC conductivity evaluated using the generalized Nernst–Einstein equation
s^{Jo}	Dimensionless exponent governing the degree of dispersion
T	Temperature
t	Time
τ	Timescale of interest
τ^{HM}	Relaxation time characteristic of the Havriliak–Negami process
$\tau_i = R_iC_i$	Relaxation time associated with branch (i)
V	the volume probed
$\vec{v}_i$	Velocities of particles during molecular simulations
Z; Z', Z''	Impedance, real and imaginary part of the impedance
Z_{bulk}	Contribution of bulk electrolytes to the total impedance Z
Z_{int}	Contribution of interfaces to the total impedance Z
Z_{CPE}	Impedance of the constant phase element (CPE)
z_i	Charge number of ion i

List of symbols

See Table 6.

CRediT authorship contribution statement

Tulio Honorio: Writing – review & editing, Writing – original draft, Visualization, Validation, Supervision, Methodology, Investigation, Formal analysis, Conceptualization. **Walter Batista Bonfim:** Writing – review & editing, Writing – original draft, Investigation, Formal analysis. **Oswaldo Cascudo:** Writing – review & editing, Supervision, Resources, Conceptualization.

Declaration of Generative AI and AI-assisted technologies in the writing process

During the preparation of this work the authors used ChatGPT in order to improve language and readability. After using this tool/service, the authors reviewed and edited the content as needed and take full responsibility for the content of the publication.

Declaration of competing interest

The authors declare that they have no known competing financial interests or personal relationships that could have appeared to influence the work reported in this paper.

Acknowledgments

Eletrobras Furnas and the agency ANEEL - Agência Nacional de Energia Elétrica, from Brazil, are gratefully acknowledged for their financial support. O. Cascudo also thanks CNPq - Conselho Nacional de Desenvolvimento Científico e Tecnológico, from Brazil, which provided a research grant.

Appendix A. Supplementary data

Supplementary material related to this article can be found online at https://doi.org/10.1016/j.cemconres.2025.108123.

Data availability

Data will be made available on request.

References

[1] R.T. Coverdale, B.J. Christensen, H.M. Jennings, T.O. Mason, D.P. Bentz, E.J. Garboczi, Interpretation of impedance spectroscopy of cement paste via computer modelling, J. Mater. Sci. 30 (3) (1995) 712–719, http://dx.doi.org/10.1007/BF00356331.

[2] T. Honorio, H. Carasek, O. Cascudo, Electrical properties of cement-based materials: Multiscale modeling and quantification of the variability, Constr. Build. Mater. 245 (2020) 118461, http://dx.doi.org/10.1016/j.conbuildmat.2020.118461, URL http://www.sciencedirect.com/science/article/pii/S0950061820304669.

[3] E.J. Garboczi, D.P. Bentz, Computer simulation of the diffusivity of cement-based materials, J. Mater. Sci. 27 (8) (1992) 2083–2092, http://dx.doi.org/10.1007/BF01117921.

[4] E.J. Garboczi, D.P. Bentz, Modelling of the microstructure and transport properties of concrete, Constr. Build. Mater. 10 (5) (1996) 293–300, http://dx.doi.org/10.1016/0950-0618(94)00019-0, URL http://www.sciencedirect.com/science/article/pii/0950061894000190.

[5] H. Ma, D. Hou, J. Liu, Z. Li, Estimate the relative electrical conductivity of C–S–H gel from experimental results, Constr. Build. Mater. 71 (2014) 392–396, http://dx.doi.org/10.1016/j.conbuildmat.2014.08.036, URL http://www.sciencedirect.com/science/article/pii/S0950061814009477.

[6] Z. Liu, Y. Zhang, L. Liu, Q. Jiang, An analytical model for determining the relative electrical resistivity of cement paste and C–S–H gel, Constr. Build. Mater. 48 (2013) 647–655, http://dx.doi.org/10.1016/j.conbuildmat.2013.07.020, URL https://www.sciencedirect.com/science/article/pii/S095006181300634X.

[7] R.O. Agbaoye, J. Janovec, A. Ayuela, J.S. Dolado, Thermoelectric properties of the main species present in Portland cement pastes, Cem. Concr. Res. 183 (2024) 107587, http://dx.doi.org/10.1016/j.cemconres.2024.107587, URL https://www.sciencedirect.com/science/article/pii/S0008884624001686.

[8] T. Honorio, Monte Carlo molecular modeling of temperature and pressure effects on the interactions between crystalline calcium silicate hydrate layers, Langmuir 35 (11) (2019) 3907–3916, http://dx.doi.org/10.1021/acs.langmuir.8b04156, URL https://pubs.acs.org/doi/10.1021/acs.langmuir.8b04156.

[9] R.J.M. Pellenq, N. Lequeux, H. van Damme, Engineering the bonding scheme in C–S–H: The iono-covalent framework, Cem. Concr. Res. 38 (2) (2008) 159–174, http://dx.doi.org/10.1016/j.cemconres.2007.09.026, URL http://www.sciencedirect.com/science/article/pii/S0008884607002372.

[10] C. Andrade, R. d'Andrea, N. Rebolledo, Chloride ion penetration in concrete: The reaction factor in the electrical resistivity model, Cem. Concr. Compos. 47 (2014) 41–46, http://dx.doi.org/10.1016/j.cemconcomp.2013.09.022, URL https://www.sciencedirect.com/science/article/pii/S0958946513001583.

[11] S. Grangeon, F. Claret, C. Roosz, T. Sato, S. Gaboreau, Y. Linard, Structure of nanocrystalline calcium silicate hydrates: insights from X-ray diffraction, synchrotron X-ray absorption and nuclear magnetic resonance, J. Appl. Crystallogr. 49 (Pt 3) (2016) 771–783, http://dx.doi.org/10.1107/S1600576716003885, URL http://www.ncbi.nlm.nih.gov/pmc/articles/PMC4886978/.

[12] A. Cuesta, J.D. Zea-Garcia, D. Londono-Zuluaga, A.G.D.l. Torre, I. Santacruz, O. Vallcorba, M. Dapiaggi, S.G. Sanfélix, M.A.G. Aranda, Multiscale understanding of tricalcium silicate hydration reactions, Sci. Rep. 8 (1) (2018) 1–11, http://dx.doi.org/10.1038/s41598-018-26943-y, URL https://www.nature.com/articles/s41598-018-26943-y.

[13] T. Honorio, H. Carasek, O. Cascudo, May self-diffusion of ions computed from molecular dynamics explain the electrical conductivity of pore solutions in cement-based materials? Mater. Struct. 53 (3) (2020) 67, http://dx.doi.org/10.1617/s11527-020-01507-7.

[14] J.M. Caillol, D. Levesque, J.J. Weis, Theoretical calculation of ionic solution properties, J. Chem. Phys. 85 (11) (1986) 6645–6657, http://dx.doi.org/10.1063/1.451446, URL https://aip.scitation.org/doi/abs/10.1063/1.451446.

[15] K.F. Rinne, S. Gekle, R.R. Netz, Dissecting ion-specific dielectric spectra of sodium-halide solutions into solvation water and ionic contributions, J. Chem. Phys. 141 (21) (2014) 214502, http://dx.doi.org/10.1063/1.4901927, URL http://aip.scitation.org/doi/10.1063/1.4901927.

[16] M. Youssef, R.J.-M. Pellenq, B. Yildiz, Glassy nature of water in an ultraconfining disordered material: The case of calcium-silicate-hydrate, J. Am. Chem. Soc. 133 (8) (2011) 2499–2510, http://dx.doi.org/10.1021/ja107003a.

[17] M.J.A. Qomi, M. Bauchy, F.-J. Ulm, R.J.-M. Pellenq, Anomalous composition-dependent dynamics of nanoconfined water in the interlayer of disordered calcium-silicates, J. Chem. Phys. 140 (5) (2014) 054515, http://dx.doi.org/10.1063/1.4864118, URL http://scitation.aip.org/content/aip/journal/jcp/140/5/10.1063/1.4864118.

[18] T. Honorio, H. Carasek, O. Cascudo, Water self-diffusion in C-S-H: Effect of confinement and temperature studied by molecular dynamics, Cem. Concr. Res. 155 (2022) 106775, http://dx.doi.org/10.1016/j.cemconres.2022.106775, URL https://www.sciencedirect.com/science/article/pii/S0008884622000667.

[19] T. Honorio, Permeability of C-S-H, Cem. Concr. Res. 176 (2024) 107408, http://dx.doi.org/10.1016/j.cemconres.2023.107408, URL https://www.sciencedirect.com/science/article/pii/S000888462300323X.

[20] S. Ait Hamadouche, T. Honorio, T. Bore, F. Benboudjema, F. Daout, E. Vourc'h, Dielectric permittivity of C-S-H, Cem. Concr. Res. 169 (2023) 107178, http://dx.doi.org/10.1016/j.cemconres.2023.107178, URL https://www.sciencedirect.com/science/article/pii/S0008884623000923.

[21] X. Hu, C. Shi, X. Liu, J. Zhang, G. de Schutter, A review on microstructural characterization of cement-based materials by AC impedance spectroscopy, Cem. Concr. Compos. 100 (2019) 1–14, http://dx.doi.org/10.1016/j.cemconcomp.2019.03.018, URL https://www.sciencedirect.com/science/article/pii/S0958946518304529.

[22] B.J. Christensen, T. Coverdale, R.A. Olson, S.J. Ford, E.J. Garboczi, H.M. Jennings, T.O. Mason, Impedance spectroscopy of hydrating cement-based materials: Measurement, interpretation, and application, J. Am. Ceram. Soc. 77 (11) (1994) 2789–2804, http://dx.doi.org/10.1111/j.1151-2916.1994.tb04507.x, URL https://ceramics.onlinelibrary.wiley.com/doi/abs/10.1111/j.1151-2916.1994.tb04507.x.

[23] C. Andrade, V.M. Blanco, A. Collazo, M. Keddam, X.R. Nóvoa, H. Takenouti, Cement paste hardening process studied by impedance spectroscopy, Electrochim. Acta 44 (24) (1999) 4313–4318, http://dx.doi.org/10.1016/S0013-4686(99)00147-4, URL http://www.sciencedirect.com/science/article/pii/S0013468699001474.

[24] A.F. Sosa Gallardo, J.L. Provis, Early-age characterisation of Portland cement by impedance spectroscopy, Adv. Cem. Res. (2022) 1–36, http://dx.doi.org/10.1680/jadcr.21.00103, URL https://www.icevirtuallibrary.com/doi/abs/10.1680/jadcr.21.00103.

[25] P. Gu, P. Xie, Y. Fu, J.J. Beaudoin, A.C impedance phenomena in hydrating cement systems: Frequency dispersion angle and pore size distribution, Cem. Concr. Res. 24 (1) (1994) 86–88, http://dx.doi.org/10.1016/0008-8846(94)90086-8, URL https://www.sciencedirect.com/science/article/pii/0008884694900868.

[26] Z. Zhang, Q. You, Y. Hu, G. Geng, Anomalous time-constant on mortar/electrolyte interface and its influence on LPR and EIS measurement of rebar corrosion, Cem. Concr. Res. 196 (2025) 107930, http://dx.doi.org/10.1016/j.cemconres.2025.107930, URL https://www.sciencedirect.com/science/article/pii/S0008884625001498.

[27] R. Wang, F. He, C. Shi, D. Zhang, C. Chen, L. Dai, AC impedance spectroscopy of cement - based materials: measurement and interpretation, Cem. Concr. Compos. 131 (2022) 104591, http://dx.doi.org/10.1016/j.cemconcomp.2022.104591, URL https://www.sciencedirect.com/science/article/pii/S0958946522001858.

[28] R. Kubo, Statistical-mechanical theory of irreversible processes. I. general theory and simple applications to magnetic and conduction problems, J. Phys. Soc. Japan 12 (6) (1957) 570–586, http://dx.doi.org/10.1143/JPSJ.12.570, URL https://journals.jps.jp/doi/10.1143/JPSJ.12.570.

[29] V. Ballenegger, J.-P. Hansen, Dielectric permittivity profiles of confined polar fluids, J. Chem. Phys. 122 (11) (2005) 114711, http://dx.doi.org/10.1063/1.1845431, URL https://aip.scitation.org/doi/abs/10.1063/1.1845431.

[30] H.A. Stern, S.E. Feller, Calculation of the dielectric permittivity profile for a nonuniform system: Application to a lipid bilayer simulation, J. Chem. Phys. 118 (7) (2003) 3401, http://dx.doi.org/10.1063/1.1537244, URL https://aip.scitation.org/doi/abs/10.1063/1.1537244.

[31] I. Maruyama, G. Igarashi, K. Matsui, N. Sakamoto, Hinderance of C-S-H sheet piling during first drying using a shrinkage reducing agent: A SAXS study, Cem. Concr. Res. 144 (2021) 106429, http://dx.doi.org/10.1016/j.cemconres.2021.106429, URL https://www.sciencedirect.com/science/article/pii/S0008884621000788.

[32] A. Kunhi Mohamed, S.C. Parker, P. Bowen, S. Galmarini, An atomistic building block description of C-S-H - Towards a realistic C-S-H model, Cem. Concr. Res. 107 (2018) 221–235, http://dx.doi.org/10.1016/j.cemconres.2018.01.007, URL http://www.sciencedirect.com/science/article/pii/S0008884617302533.

[33] R.T. Cygan, J.A. Greathouse, A.G. Kalinichev, Advances in clayff molecular simulation of layered and nanoporous materials and their aqueous interfaces, J. Phys. Chem. C (2021) http://dx.doi.org/10.1021/acs.jpcc.1c04600.

[34] R.T. Cygan, J.-J. Liang, A.G. Kalinichev, Molecular models of hydroxide, oxyhydroxide, and clay phases and the development of a general force field, J. Phys. Chem. B 108 (4) (2004) 1255–1266.

[35] H.J.C. Berendsen, J.R. Grigera, T.P. Straatsma, The missing term in effective pair potentials, J. Phys. Chem. 91 (24) (1987) 6269–6271, http://dx.doi.org/10.1021/j100308a038.

[36] T. Honorio, F. Masara, G. Huang, F. Benboudjema, Thermal, mechanical, and transport properties of C-S-H at the molecular scale: A force field benchmark, Cement (2025) 100143, http://dx.doi.org/10.1016/j.cement.2025.100143, URL https://www.sciencedirect.com/science/article/pii/S2666549225000167.

[37] F. Masara, F. Benboudjema, T. Honorio, Cavitation, hydrophilicity, and sorption hysteresis in C–S–H pores: Coupled effects of relative humidity and temperature, Langmuir 40 (52) (2024) 27286–27298, http://dx.doi.org/10.1021/acs.langmuir.4c03223.

[38] R. Shahsavari, R.J.-M. Pellenq, F.-J. Ulm, Empirical force fields for complex hydrated calcio-silicate layered materials, Phys. Chem. Chem. Phys. 13 (3) (2010) 1002–1011, http://dx.doi.org/10.1039/C0CP00516A, URL http://pubs.rsc.org/en/content/articlelanding/2011/cp/c0cp00516a.

[39] R.J.-M. Pellenq, A. Kushima, R. Shahsavari, K.J.V. Vliet, M.J. Buehler, S. Yip, F.-J. Ulm, A realistic molecular model of cement hydrates, Proc. Natl. Acad. Sci. 106 (38) (2009) 16102–16107, http://dx.doi.org/10.1073/pnas.0902180106, URL http://www.pnas.org/content/106/38/16102.

[40] I.G. Richardson, Model structures for C-(A)-S-H(I), Acta Crystallogr. Sect. B: Struct. Sci. Cryst. Eng. Mater. 70 (6) (2014) 903–923, http://dx.doi.org/10.1107/S2052520614021982, URL http://scripts.iucr.org/cgi-bin/paper?hw5035.

[41] J.A. Greathouse, R.J. O'Brien, G. Bemis, R.T. Pabalan, Molecular dynamics study of aqueous uranyl interactions with quartz (010), J. Phys. Chem. B 106 (7) (2002) 1646–1655, http://dx.doi.org/10.1021/jp013250q, URL https://pubs.acs.org/doi/10.1021/jp013250q.

[42] D. Laage, G. Stirnemann, Effect of ions on water dynamics in dilute and concentrated aqueous salt solutions, J. Phys. Chem. B 123 (15) (2019) 3312–3324, http://dx.doi.org/10.1021/acs.jpcb.9b01053, URL http://pubs.acs.org/doi/10.1021/acs.jpcb.9b01053.

[43] F. Masara, T. Honorio, F. Benboudjema, Sorption in C-S-H at the molecular level: Disjoining pressures, effective interactions, hysteresis, and cavitation, Cem. Concr. Res. 164 (2023) 107047, http://dx.doi.org/10.1016/j.cemconres.2022.107047, URL https://www.sciencedirect.com/science/article/pii/S0008884622003398.

[44] T. Honorio, F. Masara, F. Benboudjema, Heat capacity, isothermal compressibility, isosteric heat of adsorption and thermal expansion of water confined in C-S-H, Cement (2021) 100015, http://dx.doi.org/10.1016/j.cement.2021.100015, URL https://www.sciencedirect.com/science/article/pii/S2666549221000128.

[45] C. Chassagne, E. Dubois, M.L. Jiménez, J.P.M. van der Ploeg, J. van Turnhout, Compensating for electrode polarization in dielectric spectroscopy studies of colloidal suspensions: Theoretical assessment of existing methods, Front. Chem. 4 (2016) http://dx.doi.org/10.3389/fchem.2016.00030, URL https://www.frontiersin.org/journals/chemistry/articles/10.3389/fchem.2016.00030/full.

[46] G. Pireddu, C.J. Fairchild, S.P. Niblett, S.J. Cox, B. Rotenberg, Impedance of nanocapacitors from molecular simulations to understand the dynamics of confined electrolytes, Proc. Natl. Acad. Sci. 121 (18) (2024) e2318157121, http://dx.doi.org/10.1073/pnas.2318157121, URL https://www.pnas.org/doi/10.1073/pnas.2318157121.

[47] A.P. Thompson, H.M. Aktulga, R. Berger, D.S. Bolintineanu, W.M. Brown, P.S. Crozier, P.J. in 't Veld, A. Kohlmeyer, S.G. Moore, T.D. Nguyen, R. Shan, M.J. Stevens, J. Tranchida, C. Trott, S.J. Plimpton, LAMMPS - a flexible simulation tool for particle-based materials modeling at the atomic, meso, and continuum scales, Comput. Phys. Comm. 271 (2022) 108171, http://dx.doi.org/10.1016/j.cpc.2021.108171, URL https://www.sciencedirect.com/science/article/pii/S0010465521002836.

[48] R. Metzler, J.-H. Jeon, A.G. Cherstvy, E. Barkai, Anomalous diffusion models and their properties: non-stationarity, non-ergodicity, and ageing at the centenary of single particle tracking, Phys. Chem. Chem. Phys. 16 (44) (2014) 24128–24164, http://dx.doi.org/10.1039/C4CP03465A, URL http://xlink.rsc.org/?DOI=C4CP03465A.

[49] T. Honorio, Power-law creep in C-S-H c-s-h emerging from subdiffusive dynamics, 2026.

[50] A. Jaishankar, G.H. McKinley, Power-law rheology in the bulk and at the interface: quasi-properties and fractional constitutive equations, Proc. R. Soc. A: Math. Phys. Eng. Sci. 469 (2149) (2013) 20120284, http://dx.doi.org/10.1098/rspa.2012.0284, URL https://royalsocietypublishing.org/doi/10.1098/rspa.2012.0284.

[51] T. Honorio, M. Trifa, T. Herin, S. Le Caër, H2 anisotropic subdiffusion and induced expansion in portlandite, gibbsite, and boehmite, J. Phys. Chem. C 128 (45) (2024) 19085–19097, http://dx.doi.org/10.1021/acs.jpcc.4c04681.

[52] J.P. Boon, S. Yip, Molecular Hydrodynamics, Courier Corporation, 1991.

[53] S. Torquato, Random Heterogeneous Materials: Microstructure and Macroscopic Properties, Springer Science & Business Media, 2002.

[54] H. Hatta, M. Taya, Effective thermal conductivity of a misoriented short fiber composite, J. Appl. Phys. 58 (7) (1985) 2478–2486, http://dx.doi.org/10.1063/1.335924, URL http://aip.scitation.org/doi/10.1063/1.335924.

[55] J.C. Dyre, T.B. Schrøder, Universality of ac conduction in disordered solids, Rev. Modern Phys. 72 (3) (2000) 873–892, http://dx.doi.org/10.1103/RevModPhys.72.873.

[56] A.K. Jonscher, The 'universal' dielectric response, Nat. 267 (5613) (1977) 673–679, http://dx.doi.org/10.1038/267673a0, URL https://www.nature.com/articles/267673a0.

[57] J.C. Dyre, The random free-energy barrier model for ac conduction in disordered solids, J. Appl. Phys. 64 (5) (1988) 2456–2468, http://dx.doi.org/10.1063/1.341681.

[58] S. Havriliak, S. Negami, A complex plane representation of dielectric and mechanical relaxation processes in some polymers, Polym. 8 (1967) 161–210, http://dx.doi.org/10.1016/0032-3861(67)90021-3, URL https://www.sciencedirect.com/science/article/pii/0032386167900213.

[59] T. Honorio, T. Bore, F. Benboudjema, E. Vourc'h, M. Ferhat, Dielectric properties of the pore solution in cement-based materials, J. Mol. Liq. 302 (2020) 112548, http://dx.doi.org/10.1016/j.molliq.2020.112548, URL http://www.sciencedirect.com/science/article/pii/S0167732219360593.

[60] J. Bisquert, A. Compte, Theory of the electrochemical impedance of anomalous diffusion, J. Electroanal. Chem. 499 (1) (2001) 112–120, http://dx.doi.org/10.1016/S0022-0728(00)00497-6, URL https://www.sciencedirect.com/science/article/pii/S0022072800004976.

[61] S. Soyer-Uzun, S.R. Chae, C.J. Benmore, H.-R. Wenk, P.J.M. Monteiro, Compositional evolution of calcium silicate hydrate (C–S–H) structures by total X-ray scattering, J. Am. Ceram. Soc. 95 (2) (2012) 793–798, http://dx.doi.org/10.1111/j.1551-2916.2011.04989.x, URL https://ceramics.onlinelibrary.wiley.com/doi/abs/10.1111/j.1551-2916.2011.04989.x.

[62] S. De Luca, S.K. Kannam, B.D. Todd, F. Frascoli, J.S. Hansen, P.J. Daivis, Effects of confinement on the dielectric response of water extends up to mesoscale dimensions, Langmuir 32 (19) (2016) 4765–4773, http://dx.doi.org/10.1021/acs.langmuir.6b00791.

[63] G. Constantinides, F.-J. Ulm, The nanogranular nature of C–S–H, J. Mech. Phys. Solids 55 (1) (2007) 64–90, http://dx.doi.org/10.1016/j.jmps.2006.06.003, URL http://www.sciencedirect.com/science/article/pii/S0022509606001062.

[64] A.C.A. Muller, K.L. Scrivener, A.M. Gajewicz, P.J. McDonald, Densification of C–S–H measured by 1H NMR relaxometry, J. Phys. Chem. C 117 (1) (2012) 403–412, http://dx.doi.org/10.1021/jp3102964.

[65] M. Königsberger, C. Hellmich, B. Pichler, Densification of C-S-H is mainly driven by available precipitation space, as quantified through an analytical cement hydration model based on NMR data, Cem. Concr. Res. 88 (2016) 170–183, http://dx.doi.org/10.1016/j.cemconres.2016.04.006, URL http://www.sciencedirect.com/science/article/pii/S0008884616303374.

[66] E. Masoero, G. Cusatis, G. Di Luzio, C–s–h gel densification: The impact of the nanoscale on self-desiccation and sorption isotherms, Cem. Concr. Res. 109 (2018) 103–119, http://dx.doi.org/10.1016/j.cemconres.2018.04.014, URL https://www.sciencedirect.com/science/article/pii/S0008884617309079.

[67] A. Vollpracht, B. Lothenbach, R. Snellings, J. Haufe, The pore solution of blended cements: a review, Mater. Struct. 49 (8) (2016) 3341–3367, http://dx.doi.org/10.1617/s11527-015-0724-1.